Revision 2

Characterizing a new type of nelsonite recognized in the Damiao anorthosite complex, North China Craton, with implications for the genesis of giant magmatic Fe-Ti oxide deposits

LI-XING LI[1*], JIAN-WEI ZI[2, 3], HOU-MIN LI[1], JIE MENG[4]

[1] MNR Key Laboratory of Metallogeny and Mineral Assessment, Institute of Mineral Resources, Chinese Academy of Geological Sciences, Beijing 100037, China

[2] State Key Laboratory of Geological Processes and Mineral Resources, School of Earth Sciences, China University of Geosciences, Wuhan 430074, China

[3] John de Laeter Centre, Curtin University, Perth, WA 6102, Australia

[4] Development and Research Center of China Geological Survey, Beijing 100037, China

E-mail: lilixing1984@sina.com. Orcid 0000-0001-9988-0535

ABSTRACT

Nelsonite (Fe–Ti oxide–apatite rock) devoid of silicates offers a rare opportunity to investigate the magma processes for the formation of magmatic Fe–Ti oxide deposits. Both fractional crystallization and liquid immiscibility have been put forward, but the lack of robust evidences has hindered unambiguously distinguishing the role of these two processes in Fe–Ti mineralization. The nelsonite and associated Fe–Ti–P-rich rocks hosted in the Proterozoic Damiao anorthosite complex represent a typical example for studying Fe–Ti ore-forming processes. We recognized a new type of nelsonite (type-I) in

the Damiao complex, which is distinct from the two known types of nelsonite (type-II and III) from the same complex. The type-I nelsonite is characterized by its coexistence with oxide–apatite gabbronorite and granite in the same dike, and all these rocks have identical emplacement ages (1740 ± 7 Ma), subparallel REE patterns and major-element compositions lacking intermediate contents, suggesting derivation from conjugate Fe- and Si-rich melts generated by liquid immiscibility. The large type-II nelsonite bodies form irregular dikes along fractures in anorthosite and constitute the major ore type. The type-III nelsonite occurs as conformable layers or pods within oxide–apatite gabbronorite and pyroxenite, and occupies the end part of the type-II dike. The latter two types of nelsonites formed by extensive fractional crystallization of residual magma with crystal accumulation and subsequent hydrothermal replacement. During residual magma evolution, liquid immiscibility was crucial for Fe–Ti–P enrichment, fractional crystallization was responsible for enhancing oxide-apatite concentrations, and hydrothermal replacement was effective for mobilizing oxide-apatite concentrations. Our newly recognized nelsonite provides an unambiguous, outcrop-scale, field evidence for the operation of liquid immiscibility process. We show that giant magmatic Fe–Ti oxide orebodies can form by a combination of processes involving liquid immiscibility, fractional crystallization and hydrothermal mobilization.

Keyword Fe–Ti oxide deposits Nelsonite Liquid immiscibility Fractional crystallization Anorthosite

INTRODUCTION

Magmatic Fe–Ti oxide deposits associated with mafic layered intrusions and Proterozoic anorthosite complexes are important sources of iron, titanium and vanadium. Large Fe–Ti oxide orebodies represent extreme differentiation products of tholeiitic basalt magma, but the magmatic processes responsible for producing these oxide concentrations have been an enduring problem in economic geology and igneous petrology (Bowen 1928; Ashwal 1993; Duchesne 1999; Veksler 2009; Namur et al. 2012; Charlier et al. 2015; Bai et al. 2021). Nelsonite (Fe–Ti oxide–apatite rock) (Watson and Taber 1910) devoid of silicates constitutes an important ore type of the Fe–Ti oxide deposits, and has been widely regarded as a unique rock type critical for understanding the magma processes leading to Fe–Ti mineralization (Philpotts 1967; Kolker 1982; Tollari et al. 2008; Duchesne and Liégeois 2015).

Most nelsonite occurs in close association with Proterozoic anorthosite complexes, and generally form veins or dikes cross-cutting surrounding anorthosite, but sometimes also occurs as conformable layers within Fe–Ti oxide-rich silicate rocks (Ashwal 1993; Duchesne 1999; Zhang 2018). The origin of nelsonite remains enigmatic. The cross-cutting relationship and experimental results have led many researchers to consider an origin from crystallization of Fe–Ti–P-rich melt segregated from its Si-rich immiscible conjugate (Philpotts 1967; Kolker 1982; VanTongeren and Mathez 2012; Zhou et al. 2013; Wang et al. 2018; Coint et al. 2020), whereas others attribute the formation of such ore bodies to extensive fractional crystallization associated with crystal sorting and accumulation from a homogenous melt on the basis of their conformable occurrences (Dymek and Owens 2001; Pang et al. 2008; Song et al. 2013; Lindsley and Epler 2017). This discrepancy is largely due to the difficulty in distinguishing the role of fractional

crystallization and liquid immiscibility in Fe–Ti mineralization (Veksler et al. 2006; VanTongeren and Mathez 2012; Charlier et al. 2013; Kamenetsky et al. 2013; Honour et al., 2019a, b).

The ~ 1735 Ma Damiao anorthosite complex in the North China Craton offers an excellent opportunity to explore the origin of nelsonite, as it hosts abundant late-stage Fe–Ti–P-rich dikes/veins cross-cutting early-stage anorthosite, in association with transitional rock types including nelsonite, oxide–apatite gabbronorite and oxide–apatite pyroxenite (Zhao et al. 2009; Li et al. 2015a, 2019a; Zhang 2018). Both liquid immiscibility and fractional crystallization have been called upon to explain the origin of the nelsonite (Chen et al. 2013; Li et al. 2015a; He et al. 2016; Wang et al. 2017), but the lack of reliable evidences has hindered the testing of competing models. The liquid immiscibility model is supported by the vein/lense-like occurrence, net-texture and simple mineral assemblage of the nelsonite (Chen et al. 2013; He et al. 2016), but subsequent melting experiments have questioned the existence of silica-free immiscible Ca–Fe–Ti–P nelsonitic melt (Wang et al. 2017). Fractional crystallization is generally accepted to have contributed to the formation of large-scale nelsonite bodies, but this process cannot adequately explain the observation that apatite is separated from clinopyroxene that has similar density, but coexists with Fe-Ti oxides that have distinctly different densities (Zhang et al. 2021). The role of fractional crystallization and liquid immiscibility in Fe–Ti mineralization remains unclear.

In this study, we recognized a new type of nelsonite in a recently exposed mining occurrence of the Damiao anorthosite complex. We compare it with two known types of nelsonite from the Damiao complex, and present field and geochemical evidences for

93 critical evaluation of the relative role of liquid immiscibility and fractional crystallization
94 in the formation of large Fe–Ti oxide orebodies. The results and findings of this study
95 offer important insights into the genesis of magmatic Fe–Ti oxide deposits.

96 ## GEOLOGICAL BACKGROUND

97 The Damiao anorthosite complex is located in the Chengde area of the northern North
98 China Craton (Fig. 1A), where Archean to Paleoproterozoic crystalline basement is
99 overlain by Mesoproterozoic to Cenozoic cover. The Damiao complex is emplaced into
100 Neoarchean (~2.5 Ga) high-grade metamorphic rocks, and is unconformably covered by
101 Jurassic volcano–sedimentary rocks (Fig. 1B). The complex is divided into three separate
102 bodies on the basis of field occurrences, namely the Eastern, Central and Western Bodies,
103 with outcrop areas of ~30 km^2, <10 km^2 and ~80 km^2, respectively (Fig. 1B). Several
104 small late Paleozoic to Mesozoic intrusions occur to the southeast, southwest and west of
105 the complex (Fig. 1C). Baddeleyite Pb–Pb geochronology of gabbronorite and nelsonite
106 from this complex yielded crystallization ages of 1736 ± 3 Ma and 1734 ± 7 Ma,
107 respectively (Li et al. 2019a).

108 The Damiao anorthosite complex is characterized by two stages of emplacement:
109 early-stage anorthosite (85 %) and minor norite (10 %), and late-stage intrusions of
110 mangerite (4 %) and dike/vein-like Fe–Ti–P-rich rocks (1 %) into consolidated
111 anorthosite massif (Fig. 1C, 2, 3). Most of the Fe–Ti–P-rich rocks are distributed in the
112 triangle-shaped Western Body. Mangerite is restricted to the northwestern part of the
113 Western Body, and is not found in direct contact with the Fe–Ti–P-rich dikes/veins. All
114 the rock types are comagmatic and represent products of differentiation from high-Al
115 basaltic parental magma (Zhao et al. 2009; Li et al. 2015a, 2019a).

116 The majority of the early-stage anorthosite and norite have been hydrothermally
117 altered, resulting in bleached and highly friable rocks. Dark-colored, fresh to weakly
118 altered anorthosite is less common and generally forms irregular blocks within the altered
119 anorthosite. The dark-colored anorthosite consists of 85–95 % plagioclase ($An_{40–55}$, Li et
120 al. 2015a) and 5–10 % pyroxene (hypersthene and diopside) with subordinate amounts of
121 Fe–Ti oxides. The change in color of the anorthosite from dark to light during alteration
122 is attributable to the expelling of minute Fe–Ti oxide inclusions from plagioclase (Li et
123 al. 2014). Plagioclase has been replaced by a mixture of albite and clinozoisite in the
124 light-colored anorthosite.

125 The late-stage Fe–Ti–P-rich dikes crosscut the early-stage anorthosite and norite with
126 irregular but sharp boundaries (Fig. 1D, 2, 3), and have been mined for Fe and Ti for > 70
127 years. Most of these dikes are distributed in the Heishan–Dongdawa mining district of the
128 Western Body, with a total proven ore reserve of 317 million tonnes (33.5 % Fe and 8.6
129 % TiO_2) (Li et al. 2015b). The Fe–Ti–P-rich rocks comprise oxide–apatite gabbronorite,
130 oxide–apatite pyroxenite, nelsonite and massive Fe–Ti oxide ore. The oxide–apatite
131 gabbronorite consists of plagioclase (10–30 %), clinopyroxene (20–50 %), Fe–Ti oxides
132 (15–50 %), inverted pigeonite (5–20 %) and apatite (5–15 %). The oxide–apatite
133 pyroxenite consists of clinopyroxene (20–50 %), inverted pigeonite (10–20 %), Fe–Ti
134 oxides (15–35 %) and apatite (10–15 %). The nelsonite and massive Fe–Ti oxide ore are
135 composed of Fe–Ti oxides and apatite in variable modal proportions. The transition
136 between rock types is gradual.

137 ## GEOLOGY OF THE NELSONITE

138 The newly identified type-I nelsonite in the Xiaogou mining district, ~5 km north to

the Heishan–Dongdawa mining district represents a unique type characterized by its coexistence with granite and oxide–apatite gabbronorite (Fig. 2A–D, 4A–G). These rocks are developed in several elongate and irregular dike-like bodies restricted in early-stage coarse-grained norite. These dike-like bodies locally contain irregular fragments of norite. Boundaries between the dikes and enclosing norite are sharp but smoothly curved, and no alteration zone is observed (Fig. 2A–D). The largest dike extends >1 km, with thickness varying from 0.5-5 m. The granite occurs as irregular and discontinuous veins that dispersedly distributed in one or both sides of the dikes, and displays sharp contacts with nelsonite in the inner zone and norite in the outer zone (Fig. 2A). Most of the oxide–apatite gabbronorite blocks are enclosed by nelsonite with gradual or sharp contacts (Fig. 2B), and nelsonite locally forms stockworks filling fractures in the early-stage norite (Fig. 2C–D, 4B). The oxide–apatite gabbronorite consists of fine-grained plagioclase (30–40%), antiperthite (20–30%), orthopyroxene (10–20%), clinopyroxene (10–20%), Fe–Ti oxides (8–15%) and apatite (3–8%) (Fig. 4F). The granite displays coarse-grained equigranular texture and is composed of quartz (30–50%), K-feldspar (40–60%) and plagioclase (10–20%) (Fig. 4G). The type-I nelsonite is composed of generally constant modal proportions of Ti–magnetite (45–55%), ilmenite (20–30%), apatite (25–35%) and subordinate amounts of pyrite, pyrrhotite, sphalerite and zircon (Fig. 3A–E). The Ti–magnetite is characterized by trellis oxy-exsolutions of ilmenite lamellae. Apatite crystals occur as 0.5-10 mm equant, subhedral grains (Fig. 4A), or as elongate, euhedral grains varying in length from 0.1 mm to 10 mm with aspect ratio up to 10:1 (Fig. 4E). Elongate apatite crystals in the contact zone between the type-I nelsonite and norite fragments are commonly orientated parallel to the boundaries of the coarse-grained plagioclase and

orthopyroxene (Fig. 4B–D).

Most of the type-II nelsonite occur in the Heishan–Dongdawa mining district, and constitute a major ore type in the district, making up ~ 30% of the total ore reserves. They generally form orebodies as irregular dikes or veins along NE- and NW-striking fractures in the early-stage anorthosite and norite, with various shapes and sizes (Fig. 1D, 3A–C). The largest orebody has length, width and thickness up to 250 m, 50 m and 200 m, respectively. Mineralization layering is common in individual orebodies, with apatite-rich rocks (apatite up to 70%) concentrated in the upper part and near the margins, and oxide-rich rocks (<5 vol.% or no apatite) in the central and lower parts (Fig. 3B–C). Chlorite-dominated alteration is commonly developed on both sides of the contact zone between orebody and anorthosite (Fig. 3B–C). The alteration zone is characterized by a decreasing proportion of chlorite from the margin of the orebody outward into the anorthosite. The width of alteration zone is generally positively correlated with the size of the associated orebody. The type-II nelsonite is composed of variable modal proportions of Fe–Ti oxides (Ti–magnetite and minor ilmenite) and apatite, with subordinate amounts of chlorite, pyrite, aluminous spinel and zircon (Fig. 4H). Ti–magnetite is trellis-textured with ilmenite lamellae in (111) planes due to subsolidus readjustment (Fig. 4I). Apatite is euhedral and equigranular with crystal size ranging from 0.2 to 5 mm. Fluid inclusions are widely developed in apatite, and yielded homogenization temperatures of 180–420°C and salinities of 6.2–38.9 wt% NaCl equivalent (Li et al. 2010).

The type-III nelsonite adjacent to Fe–Ti–P-rich rocks either occurs as conformable layers within layered oxide–apatite pyroxenite (Fig. 3D–E), or concentrates near the end of the Fe–Ti–P-rich dikes showing gradual contacts with oxide–apatite pyroxenite (Fig.

185 3F–G). The oxide–apatite pyroxenite shows transitional contact with the oxide–apatite
186 gabbronorite (Fig. 3D, 4J–K). It has been suggested that the oxide–apatite gabbronorite
187 formed by rapid crystallization from the residual magma after anorthosite separation, and
188 the oxide–apatite pyroxenite by slow and extensive fractional crystallization of the
189 residual magma, whereas the nelsonite represents the most evolved cumulates directly
190 crystallized and segregated from the magma of oxide–apatite pyroxenite (Li et al. 2015a).
191 These rock types are gradually changed. The type-III nelsonite comprises Ti–magnetite
192 (40–60 %), ilmenite (10–30 %), apatite (10–40 %), pyroxene (clinopyroxene and inverted
193 pigeonite) (< 10 %) and subordinate amounts of chlorite, pyrite, aluminous spinel and
194 zircon. The textures of Fe–Ti oxides and apatite are similar to those of the type-II
195 nelsonite.

196 Crystallized melt inclusions in plagioclase are observed in plagioclase-rich rocks of
197 the complex, including early-stage anorthosite, type-I and III oxide–apatite gabbronorite
198 and late-stage anorthosite (Fig. 4L–O). The melt inclusions are 50–300 μm across and
199 show smooth boundaries with hosting plagioclase, suggesting a primary origin. They
200 commonly have similar mineral assemblages comprising euhedral to subhedral
201 clinopyroxene, apatite, ilmenite, magnetite, baddeleyite and chlorite (Fig. 4L–O).

202 ## SAMPLES AND ANALYTICAL METHODS

203 Samples of the type-I nelsonite (XGL-15, 5 kg) and oxide–apatite gabbronorite
204 (XG11-21, 10 kg), and granite (XG19-1, 2 kg) were collected from the largest dike in the
205 Xiaogou mining district (E117°52′11″, N41°09′46″) for geochronology. Zircon
206 separation was carried out using conventional heavy liquid and magnetic separation
207 techniques, followed by hand picking under a binocular microscope. Zircon grains

208 (including reference standards) were cast in 25-mm epoxy mounts and then polished until
209 the inner section of the grains was exposed. Individual zircon crystals were imaged by
210 scanning electron microscope (SEM) under back-scattered electron (BSE) and
211 cathodoluminescence (CL) modes to reveal their morphology and internal textures.
212 Zircon U–Pb dating of sample XGL-15 was performed using a SHRIMP II ion
213 microprobe at the Beijing SHRIMP Center, Chinese Academy of Geological Sciences.
214 The U concentrations and Pb/U ratios were calibrated using zircon standards M257 (U =
215 840 ppm; Nasdala et al. 2008) and TEMORA ($^{206}Pb/^{238}U$ age = 417 Ma; Black et al.
216 2003), respectively. Zircon U–Pb dating of sample XG11-21 was conducted using a
217 multi-collector CAMECA IMS 1280 ion microprobe at the Institute of Geology and
218 Geophysics, Chinese Academy of Sciences in Beijing. The U concentrations were
219 calibrated by zircon standard 91500 (U = 81 ppm, Wiedenbeck et al. 1995) and the Pb/U
220 ratios by zircon standard Plešovice (337 Ma, Sláma et al. 2008), and the Qinghu zircon
221 (159.5 ± 0.2 Ma, Li et al. 2013) was used as a monitor standard. Zircon U–Pb dating of
222 sample XG19-1 was carried out using a Finnigan Neptune inductively coupled plasma–
223 mass spectrometry (ICP–MS) equipped with a New Wave UP 213 laser ablation system
224 at the Institute of Mineral Resources, Chinese Academy of Geological Sciences in
225 Beijing. The zircon standards used for calibration and monitoring were 91500, Plešovice,
226 and GJ1 (610 ± 2 Ma, Elhlou et al. 2006). The beam spot was 20–30 μm in diameter.
227 Concordia diagrams and weighted mean ages were produced using the program Isoplot-3
228 (Ludwig 2012).

229 Thirteen samples were collected from the Xiaogou mining district for whole-rock
230 geochemistry, including five from the type-I nelsonite, six from the associated oxide–

231 apatite gabbronorite, and two from the associated granite. Eight samples of the type-II
232 and type-III nelsonites (four of each) were selected for apatite analysis of trace-element
233 geochemistry. Whole-rock and apatite analyses were performed at the Analytical
234 Laboratory of China National Nuclear Corporation in Beijing. Fresh samples were
235 crushed to ~200 mesh powders prior to analysis. Major elements were analyzed by a
236 scanning wavelength dispersion X-ray fluorescence (XRF) spectrometer (AB–104L,
237 PW2404), following Chinese national standard GB/T 14506.14–2010 for major element
238 analyses, with precisions generally about 1%. Trace elements were determined using an
239 ELEMENT XR ICP–MS following Chinese national standard GB/T 14506.30–2010 for
240 trace element analyses, with precisions generally better than 5 %.

241 In-situ major- and trace-element analyses were performed on 27 apatite crystals, of
242 which seven are from the type-II nelsonite, ten from the type-III nelsonite and related
243 oxide–apatite gabbronorite and pyroxenite, and another ten from the type-I nelsonite and
244 related oxide–apatite gabbronorite. Electron microprobe analyses of apatite were
245 conducted using a JEOL JXA-8230 Superprobe at the Institute of Mineral Resources,
246 Chinese Academy of Geological Sciences in Beijing. Operating conditions during the
247 quantitative analyses: accelerating voltage 15 kV, beam current 20 nA and beam size 5
248 μm. The standards used were albite for Si, hematite for Fe, $MnTiO_3$ for Mn, MgO for Mg,
249 $CaSiO_3$ for Ca, jadeite for Na and apatite for P, F and Cl. Data were corrected using the
250 atomic number-absorption-fluorescence (ZAF) software. For each sample, at least two
251 spot analyses were conducted. In situ apatite trace element compositions were obtained
252 using a New Wave Nd-YAG 193 nm laser attached to a Finnigan ELEMENT II ICP–MS
253 at the National Research Centre for Geoanalysis in Beijing. Each analysis was acquired

with a 40 μm beam size, 45 s ablation time, 7 Hz repetition rate and 70 mJ energy. The Ca contents determined by electron microprobe were used as internal standard, and the NIST610, NIST612 and ML3B-G as external standards. The analytical uncertainties were smaller than 10% for all analyzed elements.

RESULTS

Zircon U-Pb ages

Full-details of zircon U-Pb analytical results are presented in supplementary tables S1 and S2.

Zircon grains extracted from sample XGL-15 display subhedral and prismatic morphology, and are 50–200 μm long and 30–50 μm wide. All of the grains appear to be homogeneous in CL images (Fig. 5A). Twenty-two analyses on 22 grains yielded $^{207}Pb/^{206}Pb$ dates in the range of 1849–1338 Ma. These analyses have low concentrations of U from 5 to 35 ppm and Th from 2 to 79 ppm, with Th/U values varying from 0.44 to 3.72. Excluding 13 analyses that have relatively high proportions of common Pb (f_{206} > 1%) and/or high discordance (> 5%), the remaining 9 analyses give $^{207}Pb/^{206}Pb$ dates from 1783–1636 Ma with a weighted mean at 1717 ± 30 Ma (MSWD = 0.90) (Fig. 5A).

Zircon grains from sample XG11-21 show similar morphology to those from sample XGL-15. Most of the grains are homogeneous in CL images, but some show weak oscillatory zoning (Fig. 5B). Twenty analyses on 20 grains yielded $^{207}Pb/^{206}Pb$ dates from 1787 to 1712 Ma, with a weighted mean at 1750 ± 13 Ma (MSWD = 0.38) (Fig. 5B). These analyses are characterized by low proportions of common Pb (f_{206} < 0.7%), in spite of low concentrations of U (7–53 ppm) and Th (12–58 ppm), with Th/U values from 0.57 to 1.25.

Zircon grains from sample XG19-1 are subhedral and prismatic, and are 150–500 μm long and 80–200 μm wide. In CL images, most of the grains show weak oscillatory zoning (Fig. 5C). Fifty-three analyses on 53 zircon grains yielded $^{207}Pb/^{206}Pb$ dates from 1883 to 1635 Ma. They have U concentrations from 28 to 431 ppm, Th concentrations from 26 to 706 ppm, and Th/U values from 0.30 to 3.15. Excluding 13 analyses that have relatively high discordance (> 5%), the remaining 40 analyses gave $^{207}Pb/^{206}Pb$ dates ranging from 1792 Ma to 1689 Ma with a weighted mean of 1737 ± 10 Ma (MSWD = 1.13) (Fig. 5C).

Whole-rock compositions

Whole-rock geochemical data are presented in supplementary tables S3 and S4.

The type-I nelsonite is characterized by constantly high $Fe_2O_3^T$ (54.54–56.97%), TiO_2 (11.53–14.16%), CaO (13.37–15.70%) and P_2O_5 (10.39–12.36%), but low SiO_2 (0.61–2.71%), Al_2O_3 (1.62–2.70%), NaO (< 0.11%) and K_2O (< 0.06%), consistent with a mineral assemblage dominated by Fe-Ti oxides and apatite. In contrast, the granite samples have high SiO_2 (72.00–73.24%), Al_2O_3 (12.84–13.33%), Na_2O (3.24–3.36%) and K_2O (4.89–5.87%), but low $Fe_2O_3^T$ (2.15–2.67%), TiO_2 (0.24–0.45%), CaO (0.98–2.11%) and P_2O_5 (0.03–0.11%). In the binary diagrams of whole-rock major element compositions (Fig. 6), the oxide–apatite gabbronorite has compositions intermediate between the two end-members defined by the type-I nelsonite and granite. However, the gabbronorite is characterized by higher MgO (3.44–6.23 %), reflecting the presence of orthopyroxene.

Transition metals (Sc, V, Cr, Co, Ni, Cu, Zn) are strongly enriched in the type-I nelsonite and oxide–apatite gabbronorite compared with the granite (Fig. 7). Except Sc,

all transition metals are more enriched in the type-I nelsonite than in the oxide–apatite gabbronorite. The large ion lithophile elements (LILEs) display complex behavior. The Sr concentrations of the three rock types are similar, whereas Rb concentrations gradually increase from the type-I nelsonite through the oxide–apatite gabbronorite to the granite. The oxide–apatite gabbronorite and granite have similarly elevated Ba concentrations, much higher than the type-I nelsonite. For the high field strength element (HFSEs), the Si-rich granite (5.60–10.10 ppm Nb, 0.23–0.42 ppm Ta, 2.12–2.35 ppm Th, 0.25–0.34 ppm U, 328–933 ppm Zr and 7.29–19.10 ppm Hf) have similar concentrations of Nb and Ta but more abundant Th, U, Zr and Hf when compared with the Fe–Ti–P-rich type-I oxide–apatite gabbronorite (4.91–11.00 ppm Nb, 0.08–0.38 ppm Ta, 0.21–0.46 ppm Th, 0.05–0.10 ppm U, 70.5–133 ppm Zr and 2.87–5.49 ppm Hf).

These three types of coexisting dike-like rocks display chondrite-normalized REE patterns generally parallel to each other, which are characterized by enrichment of LREEs relative to HREEs (La_N/Yb_N = 5.83–14.19), similar to other rock types in the Damiao anorthosite complex (Fig. 8). The type-I nelsonite is characterized by the highest abundances of total REEs (865–979 ppm) and conspicuous negative Eu anomalies (Eu/Eu* = 0.49–0.55). The oxide–apatite gabbronorite associated with the type-I nelsonite show chondrite-normalized REE patterns similar to the oxide–apatite gabbronorite associated with the type-III nelsonite, with no significant Eu anomalies. The granite samples plot between the early-stage anorthosite and oxide–apatite gabbronorite, and also lack Eu anomalies. No obvious Ce anomalies are observed in any of the rock types of the Damiao anorthosite complex.

Apatite compositions

323 Apatite compositions are listed in supplementary table S5.

324 Apatite crystals from all of the rock types are F-rich and contains similar CaO (53.29–
325 56.30 %), P_2O_5 (39.75–41.89 %), F (2.21–4.75 %), FeO (0.02–1.03 %), SiO_2 (0.02–
326 0.27 %) and Cl (0–0.13 %), consistent with their homogenous textures shown in BSE and
327 CL images. Concentrations of other elements are close to, or below, the limits of
328 detection. The F/Cl ratios of apatite show an overall increasing trend from type-II (17–
329 392, average 156), through type-III (101–480, average 280) to type-I (88–1787, average
330 401) nelsonites.

331 Apatite from different rock types generally has parallel chondrite-normalized REE
332 patterns, characterized by enrichment of LREEs relative to HREEs with La_N/Yb_N in the
333 range of 10.0–18.8 (Fig. 9).

334 The three types of Fe–Ti–P-rich rocks are also commonly characterized by variable
335 apatite Sr contents, total REE contents and Eu anomalies, and display well-defined linear
336 trends in the total REEs vs. Sr and Eu/Eu* diagrams (Fig. 10). Apatite from the oxide–
337 apatite gabbronorite associated with the type-I nelsonite has the lowest Sr (240–480 ppm)
338 and Eu/Eu* (0.34–0.47), but the highest total REEs (3730–4702 ppm). The Sr (509–975
339 ppm) and Eu/Eu* (0.62–0.98) of apatite from the oxide–apatite gabbronorite and
340 pyroxenite associated with the type-III nelsonite are higher and more variable, but total
341 REE contents (1314–3573 ppm) are lower.

342 The three types of nelsonites have different apatite Sr and total REE contents and Eu
343 anomalies, defining continuous linear trends in the total REEs vs. Sr and Eu/Eu*
344 diagrams (Fig. 10). Apatite from the type-I nelsonite is characterized by relatively
345 constant Sr (457–680 ppm) and total REE contents (3676–5531 ppm), and prominent

346 negative Eu anomalies (Eu/Eu* = 0.44–0.55). Apatite of the type-III nelsonite exhibits
347 higher Sr (541–791 ppm) and Eu/Eu* (0.50–0.84), but lower total REE contents (1847–
348 3971 ppm). Apatite from the type-II nelsonite has highest Sr contents (699–1098 ppm)
349 and Eu/Eu* values (0.80–1.06), but lower total REE contents (1451–2865 ppm).

350 ## DISCUSSION

351 ### Comagmatic relationship of dike-like Fe–Ti–P-rich rocks

352 In the Xiaogou mining district, the type-I nelsonite, oxide–apatite gabbronorite and
353 granite occur in the same dike and are closely inter-related on the outcrop scale (Fig. 2A–
354 B). These rocks also have subparallel chondrite-normalized REE patterns (Fig. 8),
355 suggesting that they are cogenetic.

356 Zircon U–Pb geochronology of the three types of rocks yielded crystallization ages at
357 1717 ± 30 Ma, 1750 ± 13 Ma and 1737 ± 10 Ma, which are identical within errors and
358 confirm their close relationship in time. Age uncertainties of the samples are correlated
359 with U concentrations of zircon, as previously documented in Proterozoic anorthosite
360 complexes (Scoates and Chamberlain 2003; Li et al. 2019a). Since both the field
361 relationships and geochronology results indicate a synchronous formation of the three
362 types of rocks, combining the three datasets produces a weighted mean $^{207}Pb/^{206}Pb$ age at
363 1740 ± 7 Ma (MSWD = 0.93, n = 69) (Fig. 5D–E), which is considered as the best
364 estimation of the magmatic event. This age is within uncertainty of the emplacement age
365 of 1736 ± 3 Ma of the Damiao anorthosite complex, precisely constrained by baddeleyite
366 from the type-II nelsonite (Li et al. 2019a). The oxide–apatite gabbronorite associated
367 with the type-I nelsonite displays chondrite-normalized REE patterns highly analogous to
368 those of the oxide–apatite gabbronorite and pyroxenite associated with the type-III

This is the peer-reviewed, final accepted version for American Mineralogist, published by the Mineralogical Society of America.
The published version is subject to change. Cite as Authors (Year) Title. American Mineralogist, in press.
DOI: https://doi.org/10.2138/am-2022-8501. http://www.minsocam.org/

nelsonite (Fig. 8). These features are consistent with all of the dike-like Fe–Ti–P-rich rocks in the Damiao complex being originated from a residual magma after anorthosite segregation.

Formation of type-I Fe–Ti–P-rich rocks by liquid immiscibility

The binary diagrams of whole-rock major element compositions of the studied samples demonstrate significant compositional gaps in SiO_2 (47.7–72.0%), $Fe_2O_3^T$ (2.7–17.1%) and TiO_2 (0.5–3.2%) between the granite and the type-I Fe–Ti–P-rich rocks (Fig. 6).

Genetically related acidic rocks and Fe–Ti–P-rich rocks could be produced by late-stage fractional crystallization of residual magma that experienced variable felsic contamination/assimilation, as evidenced by experimental and geochemical studies (Vander Auwera et al. 1998; Bolle et al. 2003; Bybee et al. 2015). However, the $\varepsilon_{Nd}(t)$ values of the Damiao anorthosite complex are not correlated with their Th, U or K_2O contents, arguing against significant involvement of felsic contaminants (Li et al. 2019a). Also, a contaminated residual magma commonly produces a dioritic component besides acidic rocks and Fe–Ti–P-rich rocks (Bybee et al. 2015), but the studied rocks show apparent compositional gaps between granite and Fe–Ti–P-rich rocks. Therefore, this mechanism can be precluded in generating the type-I Fe–Ti–P-rich rocks and granite.

Liquid immiscibility between conjugate Fe- and Si-rich melts is an important petrogenetic process that can lead to major gaps of oxide contents, i.e., the absence of intermediate compositions (Veksler et al. 2007; Charlier et al. 2011, 2013; VanTongeren and Mathez 2012; Chen et al. 2013; Kamenetsky et al 2013; Hou and Veksler 2015). Melt inclusion and experimental studies have shown that the immiscible Fe-rich melt is

This is the peer-reviewed, final accepted version for American Mineralogist, published by the Mineralogical Society of America.
The published version is subject to change. Cite as Authors (Year) Title. American Mineralogist, in press.
DOI: https://doi.org/10.2138/am-2022-8501. http://www.minsocam.org/

392 composed of 30–50% SiO_2 and 18–32% $Fe_2O_3^T$, whereas the immiscible Si-rich melt
393 comprises 60–76% SiO_2 and 4–13% $Fe_2O_3^T$ (Jakobsen et al. 2005; Charlier and Grove
394 2012). The major element compositions of the intimately associated oxide–apatite
395 gabbronorite (41.49–47.74% SiO_2 and 17.14–24.69% $Fe_2O_3^T$) and granite (72.00–73.24%
396 SiO_2 and 2.15–2.67% $Fe_2O_3^T$) associated with the type-I nelsonite in the Xiaogou mining
397 district fit well with the assumption of two immiscible melts.

398 In this study, we chose the experimental products of Fe- and Si-rich melts of Charlier
399 and Grove (2012) for comparison because of the compositional similarities between the
400 starting materials (46–56% SiO_2 and 11.7–17.7% $Fe_2O_3^T$) and the residual magma of the
401 Damiao anorthosite complex (48.13–49.00% SiO_2 and 15.38–15.61% $Fe_2O_3^T$, Zhao et al.
402 2009) (Fig. 6). In Figure 6, the granitic samples plot exactly into the fields of the
403 experimental Si-rich melts, and the type-I oxide–apatite gabbronorite samples generally
404 fall into the fields of the experimental Fe-rich melts except for Al_2O_3, which is likely a
405 reflection of Al-spinel accumulation. The CaO/Al_2O_3 ratio is a sensitive indicator for
406 immiscibility as fractionation between the two elements is very limited (Jacobsen et al.
407 2005; Coint et al. 2020). In the SiO_2–CaO/Al_2O_3 diagram, the type-I oxide–apatite
408 gabbronorite and granite samples fall into the experimental Fe-rich and Si-rich melts,
409 respectively (Fig. 6F). Previous experiments have also demonstrated that, compared with
410 Si-rich melt, Fe-rich melt is strongly enriched in REEs , Sr and transition metals such as
411 Sc, V, Cr, Co, Ni, Cu and Zn (Watson 1976; Veksler et al. 2006; Charlier and Grove
412 2012; Lester et al. 2013a; Veksler and Charlier 2015). This feature is also observed in
413 contrasting compositions of the oxide–apatite gabbronorite (192–378 ppm REEs, 289–
414 457 ppm Sr, 24.6–38.6 ppm Sc, 199–554 ppm V, 2.2–16.8 ppm Cr, 30.6–70.8 ppm Co,

415 8.5–46.5 Ni, 31.0–55.9 ppm Cu and 186–352 ppm Zn) and granite (84–139 ppm REEs,
416 73–281 ppm Sr, 1.7–4.2 ppm Sc, 14.8–16.0 ppm V, 1.0–1.2 ppm Cr, 2.5–2.8 ppm Co,
417 1.9–2.4 Ni, 3.2–4.0 ppm Cu and 26.0–38.1 ppm Zn) associated with the type-I nelsonite
418 (Fig. 7). Collectively, these features indicate that the oxide–apatite gabbronorite and
419 granite were directly crystallized from segregated Fe-rich and Si-rich immiscible melts
420 that were evolved from the magma residual to anorthosite.

421 According to experiments, the HFSEs such as Th, U, Zr and Hf tend to concentrate in
422 the Fe-rich melt, although partition coefficients can be affected by many parameters such
423 as water content and oxygen fugacity (Watson 1976; Veksler et al. 2006; Lester et al.
424 2013b). In this study, however, the Si-rich granite has higher concentrations of Th, U, Zr
425 and Hf than the Fe–Ti–P-rich type-I oxide–apatite gabbronorite. This is unexpected, but
426 similar element behaviors have been documented elsewhere, e.g., in the Skaergaard
427 intrusion of Greenland and Raftsund intrusion of Norway where liquid immiscibility has
428 proven to be important (McBirney, 2002; Coint et al. 2020). This phenomenon can be
429 attributed to the presence of specific accessory phase of zircon, which is more abundant
430 and has higher concentrations of Th and U in the Si-rich granite than in the Fe–Ti–P-rich
431 type-I oxide–apatite gabbronorite (Fig. 5). It is noteworthy that in the type-I oxide–apatite
432 gabbronorite, Zr-bearing phase is represented initially by micron-sized baddeleyite hosted
433 in crystallized melt inclusions (Fig. 4M), and later by coarse-grained zircon (Fig. 5B),
434 reflecting enhanced input of Si during crystallization of the Fe-rich melt. This feature
435 indicates that natural silicate liquid immiscibility is likely a transient phenomenon, and
436 the segregated Fe-rich and Si-rich melts quickly hybridize as they crystallize. In this
437 process, some of the most incompatible HFSEs tend to concentrate in the more stable and

438 mobile Si-rich melt rather than the more refractory Fe-rich melt, regardless of their
439 distribution during the preceding immiscibility stage.

440 **Role of liquid immiscibility in Fe–Ti–P mineralization**

441 Some fine-grained ferrodioritic dikes at the margins of the Damiao complex contain
442 48.13–49.00% SiO_2, 15.38–15.61% $Fe_2O_3^T$, 2.29–2.72% TiO_2 and 0.31–0.35% P_2O_5, and
443 are considered to represent the residual magma of the anorthosite complex (Zhao et al.
444 2009). As expected, they appear to fill in the compositional gaps between the oxide–
445 apatite gabbronorite and granite associated with the type-I nelsonite (Fig. 6–8). Residual
446 magma evolution from the initial melt to the Fe-rich immiscible melt led to significant
447 enrichment of Fe, Ti and P, and depletion of Si and Al. Therefore, liquid immiscibility
448 probably played an important role in Fe–Ti–P enrichment during residual magma
449 evolution.

450 Liquid immiscibility has been regarded as the controlling factor for the formation of
451 nelsonite, accounting for the features of discordant veins and dikes intruding anorthosites
452 (Philpotts 1967; Kolker 1982). However, recent experimental studies have negated the
453 existence of Fe-Ti oxide melt at geologically reasonable temperatures (< 1300 °C)
454 (Lindsley and Epler 2017; Wang et al. 2017). In the present study, the intimate
455 relationship between the type-I nelsonite and the oxide–apatite gabbronorite indicates that
456 the former is also a product derived from the Fe-rich immiscible melt. This interpretation
457 is further supported by the identical morphology and chondrite-normalized REE patterns
458 of apatite from both the nelsonite and oxide–apatite gabbronorite (Fig. 4E, 4G–H, 9–10).
459 The cross-cutting relationships of the nelsonite with hosting anorthosite or norite imply
460 that it was emplaced as crystalline mush through a squeeze-out process (Ashwal 1993;

461 Duchesne 1999; Lindsley and Epler 2017). The nelsonite likely represents cumulates
462 evolved from Fe-rich immiscible melt rather than solidified Fe-rich immiscible melt, and
463 the latter is interpreted to form the fine-grained oxide–apatite gabbronorite.

464 Therefore, the coexistence of oxide–apatite gabbronorite and nelsonite formed by
465 liquid immiscibility affords an opportunity to explore the partition of elements from a
466 Fe-rich melt to nelsonite. The nelsonite is enriched in REEs and transition metal elements
467 (except for Sc), but depleted in LILE (Rb, Sr and Ba). This can be explained by early
468 segregation of Sc-rich pyroxene and Rb–Sr–Ba-rich plagioclase from the Fe-rich melt.
469 Apatite crystals from both the nelsonite and the oxide–apatite gabbronorite show similar
470 chondrite-normalized REE patterns and total REE abundances, but those from the former
471 are characterized by slightly higher Sr and less pronounced negative Eu anomalies. This
472 observation can be explained by the partition of elements between coexisting apatite and
473 plagioclase, as the latter mineral is also rich in Sr and typically has positive Eu anomalies
474 (Li et al. 2015a). Apatite from both the oxide–apatite gabbronorite and the nelsonite
475 displays similar Eu anomalies (Fig. 9, 10B), implying that fractional crystallization has
476 minimal influence on the extent of apatite Eu anomalies.

477 **Role of fractional crystallization in Fe–Ti–P mineralization**

478 Large-scale nelsonites (type-II and III) are distributed in the Heishan–Dongdawa
479 mining district. Field observations indicate that they either occur as conformable layers
480 alternating with oxide–apatite pyroxenite, or sit at the end of the Fe–Ti–P-rich dikes with
481 gradual contacts with oxide–apatite pyroxenite or oxide–apatite gabbronorite (Fig. 3D–G).
482 Whole-rock compositions of the Fe–Ti–P-rich rocks show well-defined linear trends,
483 with a Si–Al–Mg-rich end member and a Fe–Ti-rich end member (Fig. 6). This feature is

This is the peer-reviewed, final accepted version for American Mineralogist, published by the Mineralogical Society of America.
The published version is subject to change. Cite as Authors (Year) Title. American Mineralogist, in press.
DOI: https://doi.org/10.2138/am-2022-8501. http://www.minsocam.org/

484 attributable to cumulate rocks formed by two-component mixing of plagioclase–pyroxene
485 and Fe–Ti oxide members (Duchesne and Charlier 2005). As shown in Figure 6B, the
486 Al_2O_3 contents of the oxide–apatite gabbronorite and the pyroxenite can be variable and
487 are not necessarily correlated with SiO_2, suggesting that the aluminum contents in these
488 rocks are also controlled by Al-spinel (60.14–62.05% Al_2O_3 and <0.11% SiO_2, Chen et al.
489 2013) apart from plagioclase. Field and geochemical evidences support the formation of
490 large-scale nelsonite by extensive fractional crystallization with crystal accumulation.

491 The remarkable similarity in chondrite-normalized REE patterns between apatite and
492 related Fe–Ti–P-rich rocks suggests that the REE budget of each sample is largely
493 controlled by apatite (Fig. 9). Apatite crystals from all the three types of nelsonites,
494 commonly show that Eu/Eu* values (0.44–1.06) and Sr contents (457–1098 ppm) are
495 negatively correlated with their total REE contents (1451–5531 ppm), resulting in
496 continuous linear trends (Fig. 10).

497 Variable negative Eu anomalies in apatite might be attributed to crystallization under
498 different f_{O2} conditions. However, abundant nelsonites have been shown to have
499 crystallized constantly close to the FMQ buffer curve (Kolker 1982; McLelland et al.
500 1994; VanTongeren and Mathez 2012). Moreover, differences in f_{O2} conditions, typically
501 associated with variable Ce anomalies, are not observed in the apatite samples of this
502 study. Therefore, we suggest that the variation in Eu anomalies shown by the samples is
503 not related to fluctuation of oxygen fugacity.

504 Variable degrees of negative Eu anomalies in apatite can be explained by different
505 proportions of prior plagioclase crystallization from the residual melt, because
506 plagioclase is always on the liquidus in the magma parental to anorthosite suites (Ashwal

1993; Namur et al. 2011; Charlier et al. 2015). In the Damiao anorthosite complex, plagioclase in all types of plagioclase-bearing rocks is observed to be the first crystallized phase, and coarse-grained plagioclase crystals host abundant crystallized melt inclusions showing similar mineral assemblages with the interstitial melt (Fig. 4L–O). In the late-stage Fe–Ti–P-rich dikes, the Eu/Eu* values in the plagioclase aggregates (late-stage anorthosite) (0.99–2.01) are significantly higher than in the fine-grained oxide–apatite gabbronorite (0.74–1.00) (Li et al. 2015a), and thus prior crystallization of plagioclase would result in negative Eu anomalies in apatite subsequently crystallized from the residual melt. The plagioclase aggregates contain higher Sr (1025–1339 ppm vs. 285–481 ppm) but lower total REEs (51–131 ppm vs. 192–378 ppm) than the oxide–apatite gabbronorite (Li et al. 2015a). As a consequence of prior plagioclase crystallization, more REEs and less Sr would partition into apatite, a mechanism similar to the trapped liquid shift effect (Cawthorn 2013). We thus conclude that the linear trends observed in the total REEs vs. Sr and Eu/Eu* diagrams result from progressive plagioclase crystallization and Fe–Ti–P enrichment of the residual magma. This conclusion is consistent with the crystallization sequence from the oxide–apatite gabbonorite to the oxide–apatite pyroxenite associated with the type-III nelsonite, and eventually to the nelsonite as observed in the field (Li et al. 2015a).

Role of hydrothermal process in Fe–Ti–P mineralization

Extensive concentrations of Fe–Ti oxides and apatite with minor silicates cannot be simply explained by a gravity-controlled crystal sorting process, because of the similarity in density of apatite and pyroxene ($\rho_{apatite}$ = 3.1–3.3, $\rho_{Ca\text{-}poor\ pyroxene}$ = 3.4–3.7, $\rho_{Ca\text{-}rich\ pyroxene}$ = 3.3–3.5, Deer et al. 1966) making it difficult to separate the two phases by gravity.

530 Lindsley and Epler (2017) proposed that FeO–TiO_2 and P_2O_5 mutually enhance their
531 solubilities in silicate melts, and that Fe-Ti oxides and apatite tend to co-precipitate once
532 the melts become saturated with either phase. They further suggest that the cross-cutting
533 oxide-apatite bodies were probably emplaced as crystalline oxide–apatite mush, which
534 was lubricated by small amounts of residual silicate liquid to facilitate its flow.

535 The mechanism above is not able to fully explain the occurrence of large-scale
536 nelsonite in the Damiao anorthosite complex. The dikes or veins made up of nelsonite
537 and massive Fe–Ti oxide ore have depth up to 200 m (Fig. 1D, 3A), which is less likely
538 to be formed merely by a squeeze-out process. Moreover, the mineral proportions of
539 apatite and oxides in each dike or vein are highly variable, with nelsonite generally
540 distributed near the top and margin, while massive Fe–Ti oxide ore close to the bottom
541 and center (Fig. 3B–C).

542 Considering that the nelsonite dikes or veins are controlled by fractures developed in
543 early-stage anorthosite and commonly show chlorite-dominated alteration in the contact
544 zone on both sides, hydrothermal processes have probably played a part in forming these
545 features (Li et al., 2010). Based on the behavior of zirconium and silicon in magmatic–
546 hydrothermal system and fluid inclusion studies, Li et al. (2019b) proposed that the Fe–
547 Ti–P mineralization involved hydrous melts and magmatic–hydrothermal processes, with
548 the Fe–Ti oxides being formed at the magmatic stage and apatite at the hydrothermal
549 stage. Neverthe less, the substantial flow of Fe–Ti oxides along fractures appears to be
550 contradictive with the generally-held views that Ti (and Al), which is rich in nelsonite, is
551 immobile in hydrothermal fluids (Tropper and Manning 2007; Antignano and Manning
552 2008). However, Li et al. (2014) showed that Ti and Al could have been significantly

553 leached out during hydrothermal replacement of the early-stage anorthosite in the Damiao
554 complex, an interpretation similar to the magnetite flotation model proposed for the
555 Kiruna-type iron oxide-apatite deposits, which is characterized by the formation of a
556 rising oxide suspension through preferred wetting of Fe–Ti oxides in hydrothermal fluid
557 (Knipping et al. 2015, 2019).

558

559 ## IMPLICATIONS

560 The role of silicate liquid immiscibility in the petrogenesis of plutonic systems is a
561 contentious issue, and previous works in support of this process have been mainly based
562 on studies of crystal micro-structures or crystallized melt inclusions (e.g. Jakobsen et al.
563 2005; Holness et al. 2011; Borisov and Veksler, 2021). In this study, we present
564 unambiguous, outcrop-scale, field evidences for the operation of liquid immiscibility
565 process. We show that natural silicate liquid immiscibility is a transient phenomenon, and
566 hybridization of the segregated Fe-rich and Si-rich melts effectively take place during
567 their crystallization. This explains the inconsistent distribution of HFSEs such as Th, U,
568 Zr and Hf between natural samples formed by liquid immiscibility and experimental
569 immiscible melts.

570 Field relationships and geochemical characteristics of three types of nelsonites and
571 related rocks in the Proterozoic Damiao anorthosite complex reveal the important role
572 that liquid immiscibility and fractional crystallization have played in Fe–Ti–P
573 mineralization. Our new results suggest that liquid immiscibility and fractional
574 crystallization are not mutually exclusive during magma evolution, and giant magmatic
575 Fe–Ti oxide deposits probably formed by combination of these two processes. In addition,

576 hydrothermal process may also have played a role in Fe–Ti–P mineralization. The
577 Eu/Eu* value, total REEs and Sr concentrations of apatite are probably a useful indicator
578 of Fe–Ti–P mineralization.

579

580 **ACKNOWLEDGEMENTS AND FUNDING**

581 This study was financially supported by National Natural Science Foundation of China
582 (42072112, 41873062, 41402067) and Basic Research Fund of MNR Key Laboratory of
583 Metallogeny and Mineral Assessment (KK2204). We thank Xiaoxiao Ling, Jiao Li and
584 Mingyue Hu for their assistance with analyses. We appreciate Nolwenn Coint, Ilya
585 Veksler and Charles Lesher (AE) for their insightful comments and detailed suggestions
586 which helped improve the paper.

587

588 **REFERENCES CITED**

589 Antignano, A., and Manning, C.E. (2008) Rutile solubility in H_2O, H_2O-SiO_2, and
590 H_2O-$NaAlSi_3O_8$ fluids at 0.7-2.0 GPa and 700–1000 °C: Implications for mobility of
591 nominally insoluble elements. Chemical Geology, 255, 283–293.
592 Ashwal, L.D. (1993) Anorthosites. Minerals and rocks, 21. Springer, Berlin, Heidelberg,
593 83–218 pp.
594 Bai, Z.J., Zhong, H., Hu, R.Z., and Zhu, W.G. (2021) World-class Fe–Ti–V oxide
595 deposits formed in feeder conduits by removing cotectic silicates. Economic
596 Geology, 116 (3), 681–691.
597 Black, L.P., Kamo, S.L., Allen, C.M., Aleinikoff, J.N., Davis, D.W., Korsch, R.J., and
598 Foudoulis, C. (2003) TEMORA 1: a new zircon standard for Phanerozoic U–Pb

599 geochronology. Chemical Geology, 200, 155–170.
600 Bolle, O., Demaiffe, D., and Duchesne, J.C. (2003) Petrogenesis of jotunitic and acidic
601 members of an AMC suite (Rogaland anorthosite province, SW Norway): a Sr and
602 Nd isotopic assessment. Precambrian Research, 124, 185-214.
603 Borisov, A. and Veksler, I.V. (2021) Immiscible silicate liquids: K and Fe distribution as
604 a test for chemical equilibrium and insight into the kinetics of magma unmixing.
605 Contributions to Mineralogy and Petrology, 176, 47.
606 Bowen, N.L. (1928) The evolution of the igneous rocks. Princeton, New Jersey,
607 Princeton University Press, 334 pp.
608 Boynton, W.V. (1984) Geochemistry of the rare earth elements: meteorite studies. In:
609 Herderson, P. (Ed.), Rare Earth Element Geochemistry. Elservier Science Publishers
610 BV, 63–114 pp.
611 Bybee, G.M., Ashwal, L.D., Gower, C.F., and Hamilton, M.A. (2015) Pegmatitic pods in
612 the Mealy Mountains Intrusive Suite, Canada: clues to the origin of the
613 olivine-orthopyroxene dichotomy in Proterozoic Anorthosites. Journal of Petrology,
614 56(5), 845-868.
615 Cawthorn, R. (2013) Rare earth element abundances in apatite in the Bushveld
616 Complex—a consequence of the trapped liquid shift effect. Geology, 41, 603–606.
617 Charlier, B., and Grove, T. (2012) Experiments on liquid immiscibility along tholeiitic
618 liquid lines of descent. Contributions to Mineralogy and Petrology, 164, 27–44.
619 Charlier, B., Namur, O., Bolle, O., Latypov, R., and Duchesne, J.C. (2015) Fe–Ti–V–P
620 ore deposits associated with Proterozoic massif-type anorthosites and related rocks.
621 Earth Science Reviews, 141, 56–81.

622 Charlier, B., Namur, O., Grove, T. (2013) Compositional and kinetic controls on liquid
623 immiscibility in ferrobasalt–rhyolite volcanic and plutonic series. Geochimica et
624 Cosmochimica Acta, 113, 79–83.
625 Charlier, B., Namur, O., Toplis, M.J., Sciano, P., Cluzel, N., Higgins, M.D., and Vander
626 Auwera, J. (2011) Large-scale silicate liquid immiscibility during differentiation of
627 tholeiitic basalt to granite and the origin of the Daly gap. Geology, 39, 907–910.
628 Chen, W.T., Zhou, M.F., and Zhao, T.P. (2013) Differentiation of nelsonitic magmas in
629 the formation of the ~1.74 Ga Damiao Fe–Ti–P ore deposit, North China.
630 Contributions to Mineralogy and Petrology, 165(6), 1341–1362.
631 Coint, N., Keiding, J.K., and Ihlen, P.M. (2020) Evidence for silicate–liquid immiscibility
632 in monzonites and petrogenesis of associated Fe–Ti–P-rich rocks: example from the
633 Raftsund Intrusion, Lofoten, Northern Norway. Journal of Petrology, 61(4),
634 egaa045.
635 Deer, W.A., Howie, R.A., and Zussman, J. (1966) An introduction to rock-forming
636 minerals. Longmans, London, 528 pp.
637 Duchesne, J.C. (1999) Fe–Ti deposits in Rogaland anorthosites (South Norway):
638 geochemical characteristics and problems of interpretation. Mineralium Deposita, 34,
639 182–198.
640 Duchesne, J.C., Charlier, B. (2005) Geochemistry of cumulates from the
641 Bjerkreim-Sokndal layered intrusion (S. Norway). Part I: constraints from major
642 elements on the mechanism of cumu-late formation and on the jotunite liquid line of
643 descent. Lithos, 83, 229–254.
644 Duchesne, J.C., and Liégeois, J.P. (2015) The origin of nelsonite and high-Zr ferrodiorite

645 associated with Proterozoic anorthosite. Ore Geology Reviews, 71, 40–56.
646 Dymek, R., and Owens, B. (2001) Petrogenesis of apatite-rich rocks (Nelsonites and
647 Oxide–apatite gabbronorites) associated with massif anorthosites. Economic
648 Geology, 96, 797–815.
649 Elhlou, S., Belousova, E., Griffin, W.L., Pearson, N.J., and O'reilly, S.Y. (2006) Trace
650 element and isotopic composition of GJ red zircon standard by laser ablation.
651 Geochimica et Cosmochimica Acta, 70(Suppl. 1), A158.
652 He, H.L., Yu, S.Y., Song, X.Y., Du, Z.S., Dai, Z.H., Zhou, T., and Xie, W. (2016) Origin
653 of nelsonite and Fe–Ti oxides ore of the Damiao anorthosite complex, NE China:
654 evidence from trace element geochemistry of apatite, plagioclase, magnetite and
655 ilmenite. Ore Geology Reviews, 79, 367–381.
656 Holness, M.B., Stripp, G., Humphreys, M.C.S., Veksler, I.V., and Nielsen, T.F.D.
657 (2011) Silicate liquid immiscibility within the crystal mush: late-stage magmatic
658 microstructures in the Skaergaard intrusion, East Greenland. Journal of Petrology,
659 52, 175–222.
660 Honour, V.C., Holness, M.B., Partridge, J.L., and Charlier, B. (2019a) Micro-structural
661 evolution of silicate immiscible liquids in ferrobasalts. Contributions to Mineralogy
662 and Petrology, 174, 77.
663 Honour, V.C., Holness, M.B., Charlier, B., Piazolo, S.C., Namur, O., Prosa, T.J., Martin,
664 I., Helz, R.T., Maclennan, J., and Jean, M.M. (2019b) Compositional boundary
665 layers trigger liquid unmixing in a basaltic crystal mush. Nature Communiactions,
666 10(1), 1–8.
667 Hou, T., and Veksler, I.V. (2015) Experimental confirmation of high-temperature silicate

668 liquid immiscibility in multicomponent ferrobasaltic systems. American
669 Mineralogist, 100(5–6), 1304–1307.
670 Jakobsen, J.K., Veksler, I., and Tegner, C., and Brooks, C. (2005) Immiscible iron- and
671 silica-rich melts in basalt petrogenesis documented in the Skaergaard intrusion.
672 Geology 33, 885–888.
673 Kamenetsky, V.S., Charlier, B., Zhitova, L., Sharygin, V., Davidson, P., and Fein, S.
674 (2013) Magma-chamber-scale liquid immiscibility in the Siberian Traps represented
675 by melt pools in native iron. Geology 41, 1091–1094.
676 Knipping, J.L., Bilenker, L.D., Simon, A.C., Reich, M., Barra, F., Deditius, A.P.,
677 Lundstrom, C., Bindeman, I., and Munizaga, R. (2015) Giant Kiruna-type deposits
678 form by efficient flotation of magmatic magnetite suspensions. Geology 43(7), 591–
679 594.
680 Knipping, J.L., Fiege A., Simon, A.C., Oeser M., Reich, M., Bilenker, L.D. (2019) In-situ
681 iron isotope analyses reveal igneous and magmatic-hydrothermal growth of
682 magnetite at the Los Colorados Kiruna-type iron oxide-apatite deposit, Chile.
683 American Mineralogist, 104, 471–484.
684 Kolker, A. (1982) Mineralogy and geochemistry of Fe–Ti oxide and apatite (nelsonite)
685 deposits and evaluation of the liquid immiscibility hypothesis. Economic Geology
686 77(5), 1146–1158.
687 Lester, G.W., Clark, A.H., Kyser, T.K. and Naslund, H.R. (2013a). Experiments on liquid
688 immiscibility in silicate melts with H_2O, P, S, F and Cl: implications for natural
689 magmas. Contributions to Mineralogy and Petrology, 166, 329–349.
690 Lester, G.W., Kyser, T.K., Clark, A.H. and Layton-Matthews, D. (2013b). Trace element

691 partitioning between immiscible silicate melts with H_2O, P, S, F, and Cl. Chemical
692 Geology, 357, 178–185.
693 Li, H.M., Li, L.X., Zhang, Z.C., Santosh, M., Liu, M.J., Cui, Y.H., Yang, X.Q., Chen, J.,
694 and Yao, T. (2014) Alteration of the Damiao anorthosite complex in the northern
695 North China Craton: implications for high-grade iron mineralization. Ore Geology
696 Reviews, 57, 574–588.
697 Li, L.X., Li, H.M., Chen, Z.L., Wang, D.H., and Chen, W.S. (2010) Hydrothermal
698 mineralization and fluid inclusion study on the Heishan iron deposit, Chengde
699 County, Hebei province, China. Acta Petrologica Sinica, 26(3), 858–870 (in Chinese
700 with English abstract).
701 Li, L.X., Li, H.M., Li, Y.Z., Yao, T., Yang, X.Q., and Chen, J. (2015a) Origin of
702 rhythmic anorthositic–pyroxenitic layering in the Damiao anorthosite complex,
703 China: implications for late-stage fractional crystallization and genesis of Fe–Ti
704 oxide ores. Journal of Asian Earth Sciences, 113, 1035–1055.
705 Li, L.X., Li, H.M., Zi, J.W., Rasmussen, R., Sheppard, S., Ma, Y.B., Meng, J., and Song,
706 Z. (2019a) The link between an anorthosite complex and underlying olivine–
707 Ti-magnetite-rich layered intrusion in Damiao, China: insights into magma chamber
708 processes in the formation of Proterozoic massif-type anorthosites. Contributions to
709 Mineralogy and Petrology, 174, 48.
710 Li, L.X., Li, H.M., Zi, J.W., Rasmussen, R., Sheppard, S., Wilde, S.A., and Meng, J.
711 (2019b) Role of fluids in Fe–Ti–P mineralization of the Proterozoic Damiao
712 anorthosite complex, China: insights from baddeleyite–zircon relationships in ore
713 and altered anorthosite. Ore Geology Reviews, 115, 103186.

714 Li, X.H., Tang, G.Q., Gong, B., Yang, Y.H., Hou, K.J., Hu, Z.C., Li, Q.L., Liu, Y., and
715 Li, W.X. (2013) Qinghu zircon: a working reference for microbeam analysis of U–
716 Pb age and Hf and O isotopes. Chinese Science Bulletin, 58, 4647–4654.
717 Li, Y.Z., Wang, D.Z., and Li, L.X. (2015b) Metallogenetic regularity of the
718 vanadic-titano magnetite and apatite deposits in Hebei. A Monograph of the No.4
719 Team of Hebei Geological Survey, 1–182 (in Chinese).
720 Lindsley, D.H., and Epler, N. (2017) Do Fe-Ti-oxide magmas exist? Probably not!
721 American Mineralogist, 102, 2157–2169.
722 Ludwig, K.R. (2012) User's manual for Isoplot 3.75: a geochronological toolkit for
723 Microsoft Excel. In: Berkeley Geochronology Centre Special Publication, 5, 75.
724 McBirney, A.R. (2002). The Skaergaard Layered Series. Part VI. Excluded trace
725 elements. Journal of Petrology, 48, 535–556.
726 McLelland, J., Ashwal, L.D., and Moore, L. (1994) Composition and petrogenesis of
727 oxide-, apatite-rich gabbronorites associated with Proterozoic massif anorthosites:
728 examples from the Adirondack Mountains, New York. Contributions to Mineralogy
729 and Petrology, 116, 225–238.
730 Namur, O., Charlier, B., Holnes, M. (2012) Dual origin of Fe–Ti gabbros by
731 immiscibility and fractional crystallization of eveolved tholeiitic basalts in the Sept
732 Iles layered intrusion. Lithos, 154, 100–114.
733 Namur, O., Charlier, B., Pirard, C., Hermann, J., Liégeois, J.P., Vander Auwera, J. (2011).
734 Anorthosite formation by plagioclase flotation in ferrobasalt and implications for the
735 lunar crust. Geochimica et Cosmochimica Acta, 75, 4998–5018.
736 Nasdala, L., Hofmeister, W., Norberg, N., Mattinson, J.M., Corfu, F., Dor, W., Kamo,

737 S.L., Kennedy, A.K., Kronz, A., Reiners, P.W., Frei, D., Kosler, J., Wan, Y.S., Goze
738 J., Hoer, T., Kröner, A., and Valley, J.W. (2008) Zircon M257—a homogeneous
739 natural reference material for the ion microprobe U-Pb analysis of zircon.
740 Geostandards And Geoanalytical Research, 32, 247–265.
741 Pang, K.N., Li, C., Zhou, M.F., and Ripley, E.M. (2008) Abundant Fe-Ti oxide
742 inclusions in olivine from the Panzhihua and Hongge layered intrusions, SW China:
743 evidence for early saturation of Fe-Ti oxides in ferrobasaltic magma. Contributions
744 to Mineralogy and Petrology, 156, 307–321.
745 Philpotts, A.R. (1967) Origin of certain iron–titanium oxide and apatite rocks. Economic
746 Geology, 62, 303–315.
747 Scoates, J.S., and Chamberlain, K.R. (2003) Geochronologic, geochemical and isotopic
748 constraints on the origin of monzonitic and related rocks in the Laramie anorthosite
749 complex, Wyoming, USA. Precambrian Research, 124, 269–304.
750 Sláma, J., Košler, J., Condon, D.J., Crowley, J.L., Gerdes, A., Hanchar, J.M., Horstwood,
751 M.S.A., Morris, G.A., Nasdala, L., Norberg, N., Schaltegger, U., Schoene, B.,
752 Tubrett, M.N., and Whitehouse, M.J. (2008) Plešovice zircon–a new natural
753 reference material for U–Pb and Hf isotopic microanalysis. Chemical Geology, 249,
754 1–35.
755 Song, X.Y., Qi, H.W., Hu, R.Z., Chen, L.M., Yu, S.Y., and Zhang, J.F. (2013) Formation
756 of thick stratiform Fe–Ti oxide layers in layered intrusion and frequent
757 replenishment of fractionated mafic magma: evidence from the Panzhihua intrusion,
758 SW China. Geochemistry, Geophysics, Geosystems, 14(3), 712–732.
759 The 4th geological team of Hebei (2007) Geological map of the Damiao–Heishan area in

760 Chengde, China. Scale 1:25000 (in Chinese).

761 Tollari, N., Baker, D.R., and Barnes, S.J. (2008) Experimental effects of pressure and
762 fluorine on apatite saturation in mafic magmas, with reference to layered intrusions
763 and massif anorthosites. Contributions to Mineralogy and Petrology, 156, 161–175.

764 Tropper, P., and Manning, C. (2007) The solubility of corundum in H_2O at high pressure
765 and temperature and its implications for Al mobility in the deep crust and upper
766 mantle: Chemical Geology, 240, 54–60.

767 Van Tongeren, J., and Mathez, E. (2012) Large-scale liquid immiscibility at the top of the
768 Bushveld Complex, South Africa. Geology, 40, 491–494.

769 Vander Auwera, J., Longhi, J., and Duchesne, J.C. (1998) A liquid line of descent of the
770 jotunite (hypersthene monzodiorite) suite. Journal of Petrology, 39, 439–468.

771 Veksler, I., Dorfman, A., Danyushevsky, L., Jakobsen, J., and Dingwell, D. (2006)
772 Immiscible silicate liquid partition coefficients: implications for crystal-melt
773 element partitioning and basalt petrogenesis. Contributions to Mineralogy and
774 Petrology, 152, 685–702.

775 Veksler, I.V., Dorfman, A.M., Borisov, A.A., Wirth, R. and Dingwell, D.B. (2007)
776 Liquid immiscibility and evolution of basaltic magma. Journal of Petrology 48,
777 2187–2210.

778 Veksler, I.V. (2009) Extreme iron enrichment and liquid immiscibility in mafic intrusions:
779 experimental evidence revisited. Lithos, 111, 72–82.

780 Veksler, I. V. and Charlier, B. (2015) Silicate Liquid Immiscibility in Layered Intrusions.
781 In: Charlier, B., Namur, O., Latypov, R. and Tegner, C. (ed.) Layered Intrusions.
782 Berlin: Springer, pp. 229–258.

783 Wang, K., Wang, C.Y., and Ren, Z.Y. (2018) Apatite-hosted melt inclusions from the
784 Panzhihua gabbroic-layered intrusion associated with a giant Fe–Ti oxide deposit in
785 SW China: insights for magma unmixing within a crystal mush. Contributions to
786 Mineralogy and Petrology, 173, 59.
787 Wang, M., Veksler, I., Zhang, Z., Hou, T., and Keiding, J.K. (2017) The origin of
788 nelsonite constrained by melting experiment and melt inclusions in apatite: the
789 Damiao anorthosite complex, North China Craton. Gondwana Research, 42, 163–
790 176.
791 Watson, E.B. (1976) Two-liquid partition coefficients: experimental data and
792 geochemical significance. Contributions to Mineralogy and Petrology, 56, 119–134.
793 Watson, T.L., and Taber, S. (1910) Nelsonite, a new rock type; its occurrence, association,
794 and composition. Geological Society of American Bulletin, 21, 787.
795 Wiedenbeck, M., Alle, P., Corfu, F., Griffin, W.L., Meier, M., Oberli, F., Vonquadt, A.,
796 Roddick, J.C., and Speigel, W. (1995) Three natural zircon standards for U–Th–Pb,
797 Lu–Hf, trace-element and REE analyses. Geostandard Newsletter, 19, 1–23.
798 Ye, D.H. (1989) The geological setting and ore genesis of Heishan vanadic-titano
799 magnetite and apatite deposits in Chengde, Hebei. A Monograph of the No.4 Team
800 of Hebei Geological Survey, 1–355 pp (in Chinese).
801 Zhang, Z.C. (2018) Genesis of Proterozoic anorthosites and associated Fe–Ti–V–P ore
802 deposits. Bulletin of Mineralogy,Petrology and Geochemistry, 37(6), 1047–1061 (in
803 Chinese with English abstract).
804 Zhang, Z.C., Li, H.M., Li, J.W., Song, X.Y., Hu, H., Li, L.X., Chai, F.M., Hou, T., and
805 Xu, D.R. (2021) Geological settings and metallogenesis of high-grade iron deposits

in China. Science China: Earth Sciences, 64.

Zhao, G.C., Sun, M., Wilde, S.A., and Li, S.Z. (2005) Late Archean to Paleoproterozoic evolution of the North China Craton: key issues revisited. Precambrian Research, 136, 177–202.

Zhao, T.P., Chen, W., and Zhou, M.F. (2009) Geochemical and Nd–Hf isotopic constraints on the origin of the ~1.74-Ga Damiao anorthosite complex, North China Craton. Lithos, 113, 673–690.

Zhou, M.F., Chen, W.T., Wang, C.Y., Prevec, S.A., Liu, P.P., and Howarth, G.H. (2013) Two stages of immiscible liquid seperation in the formation of Panzhihua-type Fe–Ti–V oxide deposits, SW China. Geoscience Frontiers, 4, 481–502.

FIGURE CAPTIONS

Fig. 1. (A) Location of the Damiao anorthosite complex in the North China Craton (after Zhao et al. 2005). (B) Simplified geological map of the Chengde area (after Ye 1989). (C) Geological map showing the Western Body of the Damiao anorthosite complex and associated nelsonite (after the 4th geological team of Hebei 2007). (D) A profile of the Heishan–Dongdawa mining district showing the relationship between dike-like Fe–Ti–P orebodies and host anorthosite (after Li et al., 2015b).

Fig. 2. Photographs of the dike-like type-I nelsonite, type-I oxide–apatite gabbronorite and granite. (A) Type-I nelsonite coexisting with granite in a dike cross-cutting early-stage norite with smoothly curved contacts. (B) Type-I oxide–apatite gabbronorite enclosed by type-I nelsonite in a dike, with their width showing a

829 positive relationship. (C) Type-I nelsonite occurring as stockworks injecting into the
830 fractures of early-stage norite. (D) Type-I nelsonite occurring in the contact between
831 fined-grained type-I oxide–apatite gabbronorite and early-stage norite.
832
833 **Fig. 3.** Photographs of the type-II and III Fe–Ti–P-rich rocks. (A) Type-II nelsonite
834 forming irregular orebodies in the fractures of early-stage anorthosite. (B, C)
835 Development of mineralization zoning with apatite enriched in the upper level and
836 center in an orebody composed of type-II nelsonite, as well as chlorite-dominated
837 alteration on both sides of the contact zone between orebody and anorthosite. (D)
838 Type-III dike-like Fe–Ti–P-rich rocks in the fractures of early-stage anorthosite,
839 including nelsonite, oxide–apatite pyroxenite and oxide–apatite gabbronorite. (E)
840 Type-III nelsonite occurring as conformable layer within layered oxide–apatite
841 pyroxenite. (F, G) Type-III nelsonite locating in the end of Fe–Ti–P-rich-dikes.
842
843 **Fig. 4.** Photomicrographs of the type-I, II and III Fe–Ti–P-rich rocks. (A, B) Type-I
844 nelsonite showing sharp contacts with early-stage norite. (B, C) Apatite developing
845 planar orientation in the contacts between type-I nelsonite and coarse-grained
846 plagioclase and orthopyroxene of early-stage norite. (D) Chlorite replacement fronts
847 commonly developed in the contact between type-I nelsonite and early-stage norite.
848 (E) Type-I nelsonite composed of Ti-magnetite, ilmenite, apatite and minor phases
849 of zircon (Zrn) and sphalerite (Sph). (F) Oxide–apatite gabbronorite associated with
850 the type-I nelsonite containing plagioclase, antiperthite (Atp), orthopyroxene,
851 clinopyroxene, Fe–Ti oxides and apatite. (G) Granite composed of quartz (Qtz),

852 K-feldspar (Kf) and plagioclase. (H, I) Type-II nelsonite consisting of Ti-magnetite
853 (Ti-Mag), ilmenite (Ilm) and apatite. (J) Oxide–apatite gabbronorite associated with
854 the type-III nelsonite comprising plagioclase (Plag), orthopyroxene (Opx),
855 clinopyroxene (Cpx), Fe–Ti oxides and apatite (Ap). (K) Oxide–apatite pyroxenite
856 associated with the type-III nelsonite composed of clinopyroxene, Fe–Ti oxides and
857 apatite. (L–O) Crystallized melt inclusions composed of clinopyroxene (Cpx),
858 apatite (Ap), ilmenite (Ilm), magnetite (Mag), baddeleyite (Bdl) and chlorite (Chl) in
859 plagioclase (Plag) of the early-stage anorthosite (L), type-I oxide–apatite
860 gabbronorite (M), type-III oxide–apatite gabbronorite (N) and late-stage anorthosite
861 (O). A–D, F, H, J and K, plane polarized light. G, crossed polarized light. E and I,
862 reflected light. L–O, BSE image.
863
864 **Fig. 5.** (A–C) Tera-Wasserburg concordia plots of zircon U–Pb data for the type-I
865 nelsonite (XGL-15), oxide–apatite gabbronorite (XG11-21), and granite (XG19-1).
866 (D) Plots of U vs. $^{207}Pb/^{206}Pb$ ages showing correlation of age uncertainties with U
867 concentrations. (E) Age data histogram and relative probability plots of zircon.
868
869 **Fig. 6.** Binary diagrams of whole-rock major element compositions showing covariation
870 of SiO_2 vs. TiO_2, Al_2O_3, $Fe_2O_3^T$, MgO, CaO and CaO/Al_2O_3 for different dike-like
871 rock types. Our new geochemical results are plotted along with previously reported
872 data of the Fe–Ti–P-rich rocks (Zhao et al. 2009; Chen et al. 2013; Li et al. 2015a;
873 He et al. 2016) from the Heishan–Dongdawa mining district.
874

875 **Fig. 7.** Binary diagrams of whole-rock trace element compositions showing covariation
876 of Cr+V vs. Sc, Co+Ni+Cu, Rb and Sr for different dike-like rock types. Our new
877 geochemical results are plotted along with previously reported data of the Fe–Ti–
878 P-rich rocks (Zhao et al. 2009; Li et al. 2015a; He et al. 2016) from the Heishan–
879 Dongdawa mining district.
880
881 **Fig. 8.** Chondrite-normalized REE patterns of the coexisting type-I nelsonite, oxide–
882 apatite gabbronorite and granite. Gray areas representing anorthosite and type-II
883 oxide-apatite gabbronorite dikes are from Li et al. (2014, 2015a). Chondrite values
884 are from Boynton (1984).
885
886 **Fig. 9.** Chondrite-normalized REE patterns of apatite from the type-I, II and III nelsonites,
887 the oxide–apatite gabbronorite associated with the type-I nelsonite, and the oxide–
888 apatite gabbronorite and oxide–apatite pyroxenite associated with the type-III
889 nelsonite. The purple pattern representing initial residual magma (ferrodioritic dike)
890 is from Zhao et al. (2009), gray areas representing the type-III oxide–apatite
891 gabbronorite and pyroxenite are from Li et al. (2015a). Chondrite values are from
892 Boynton (1984).
893
894 **Fig. 10.** Plots of total REE vs. Eu/Eu* and Sr of apatite from the type-I, II and III
895 nelsonites, the oxide–apatite gabbronorite associated with the type-I nelsonite, and
896 the oxide–apatite gabbronorite and oxide–apatite pyroxenite associated with the
897 type-III nelsonite.

This is the peer-reviewed, final accepted version for American Mineralogist, published by the Mineralogical Society of America.
The published version is subject to change. Cite as Authors (Year) Title. American Mineralogist, in press.
DOI: https://doi.org/10.2138/am-2022-8501. http://www.minsocam.org/

Figure 1

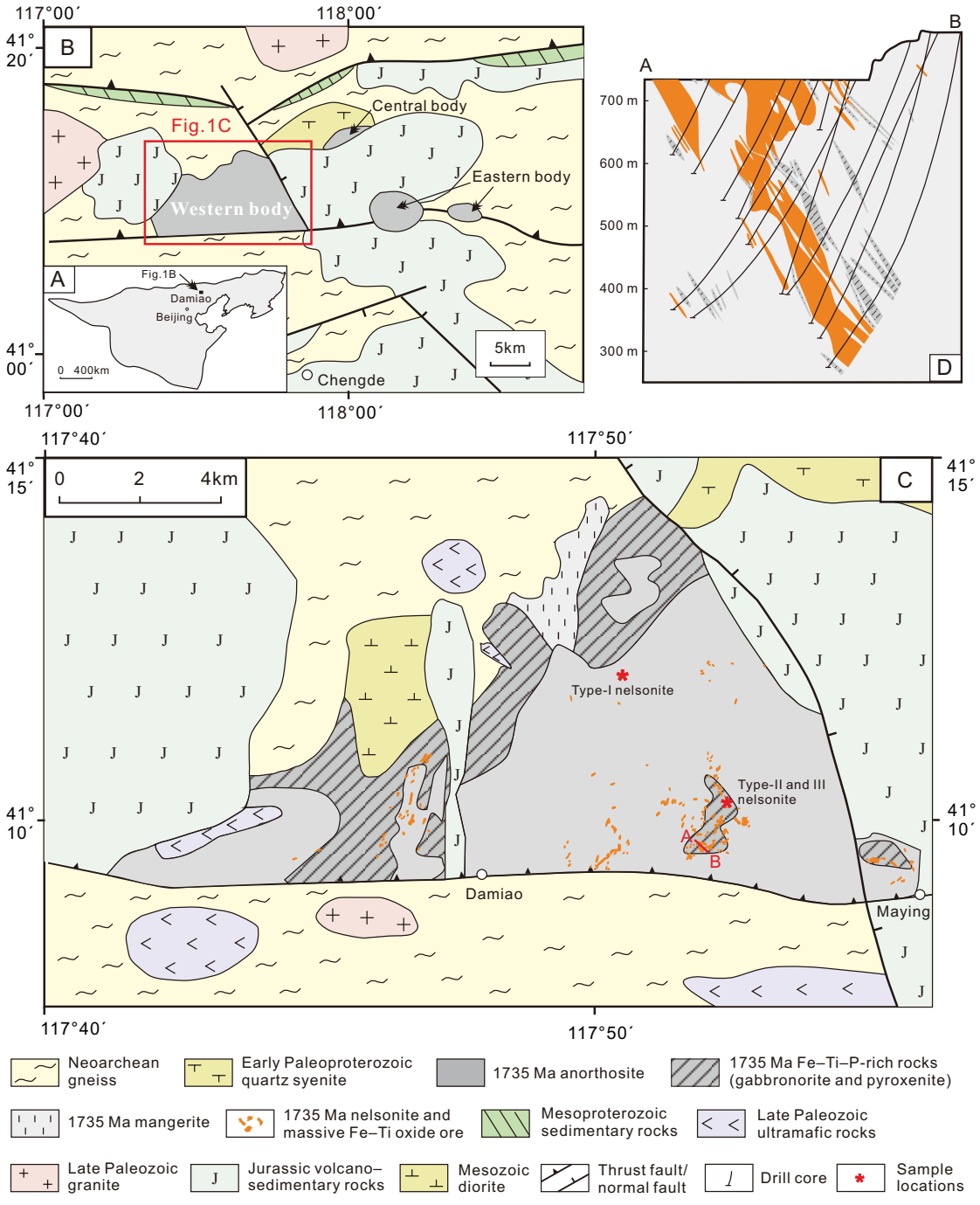

This is the peer-reviewed, final accepted version for American Mineralogist, published by the Mineralogical Society of America.
The published version is subject to change. Cite as Authors (Year) Title. American Mineralogist, in press.
DOI: https://doi.org/10.2138/am-2022-8501. http://www.minsocam.org/

Figure 2

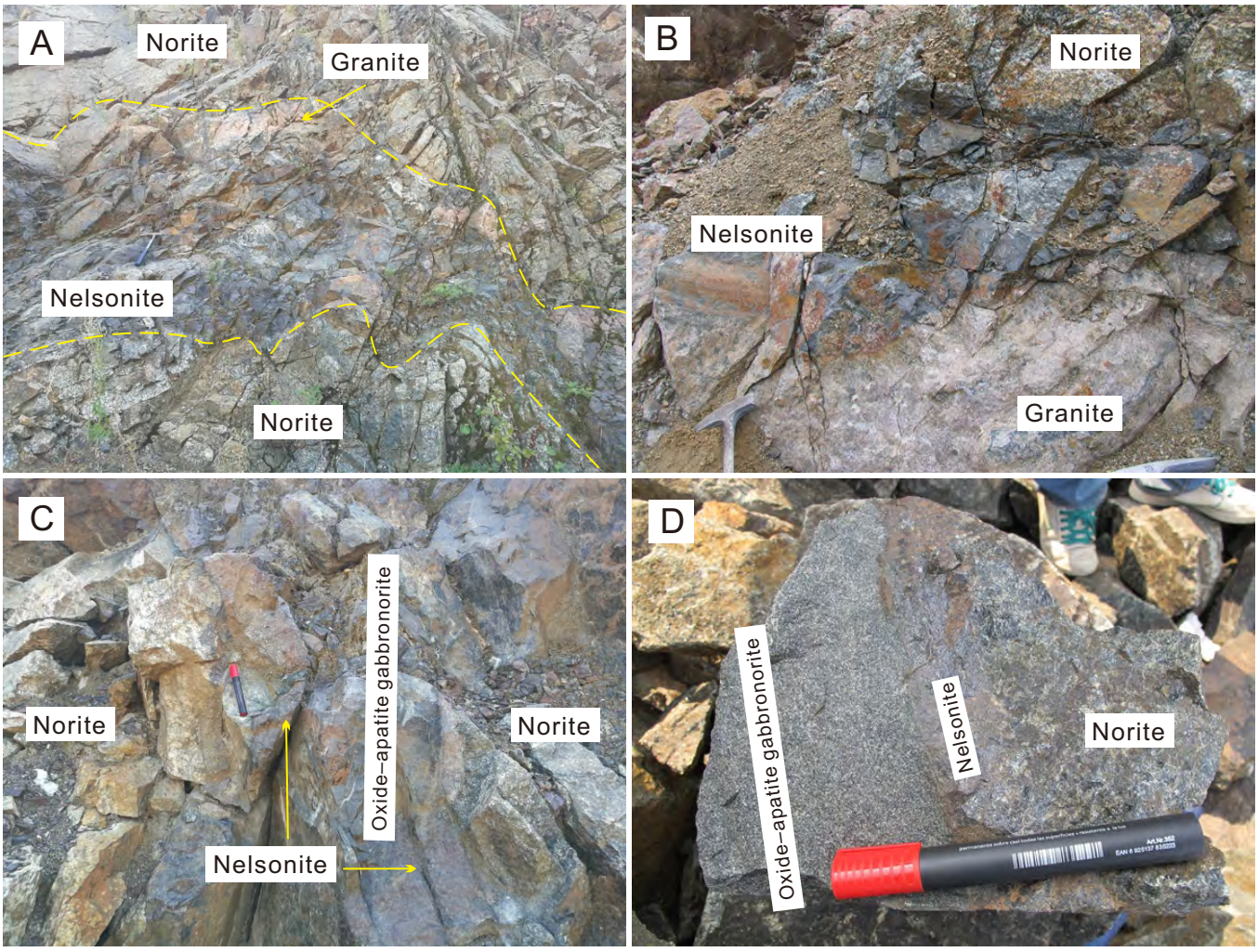

This is the peer-reviewed, final accepted version for American Mineralogist, published by the Mineralogical Society of America.
The published version is subject to change. Cite as Authors (Year) Title. American Mineralogist, in press.
DOI: https://doi.org/10.2138/am-2022-8501. http://www.minsocam.org/

Figure 3

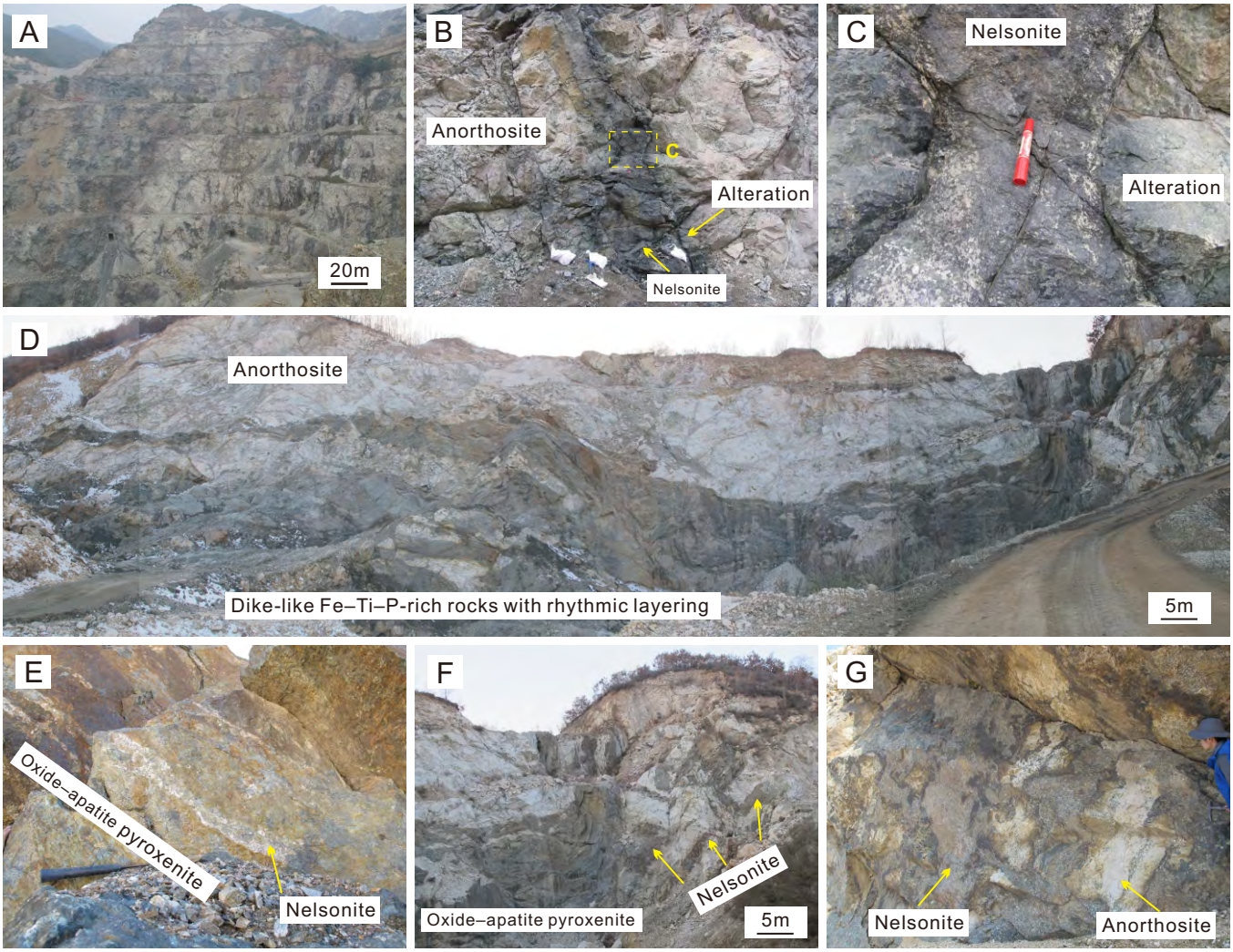

This is the peer-reviewed, final accepted version for American Mineralogist, published by the Mineralogical Society of America.
The published version is subject to change. Cite as Authors (Year) Title. American Mineralogist, in press.
DOI: https://doi.org/10.2138/am-2022-8501. http://www.minsocam.org/

Figure 4

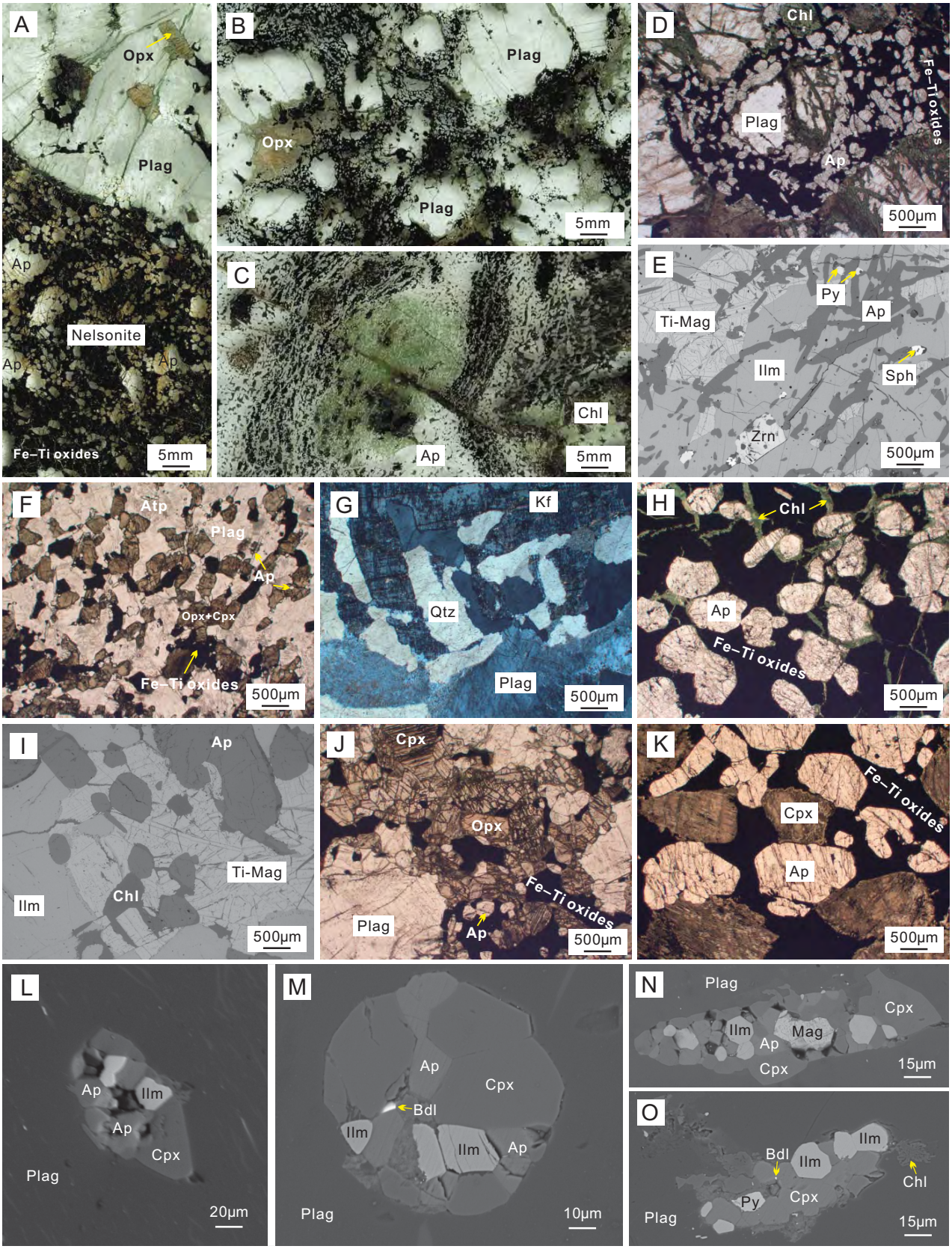

This is the peer-reviewed, final accepted version for American Mineralogist, published by the Mineralogical Society of America.
The published version is subject to change. Cite as Authors (Year) Title. American Mineralogist, in press.
DOI: https://doi.org/10.2138/am-2022-8501. http://www.minsocam.org/

Figure 5

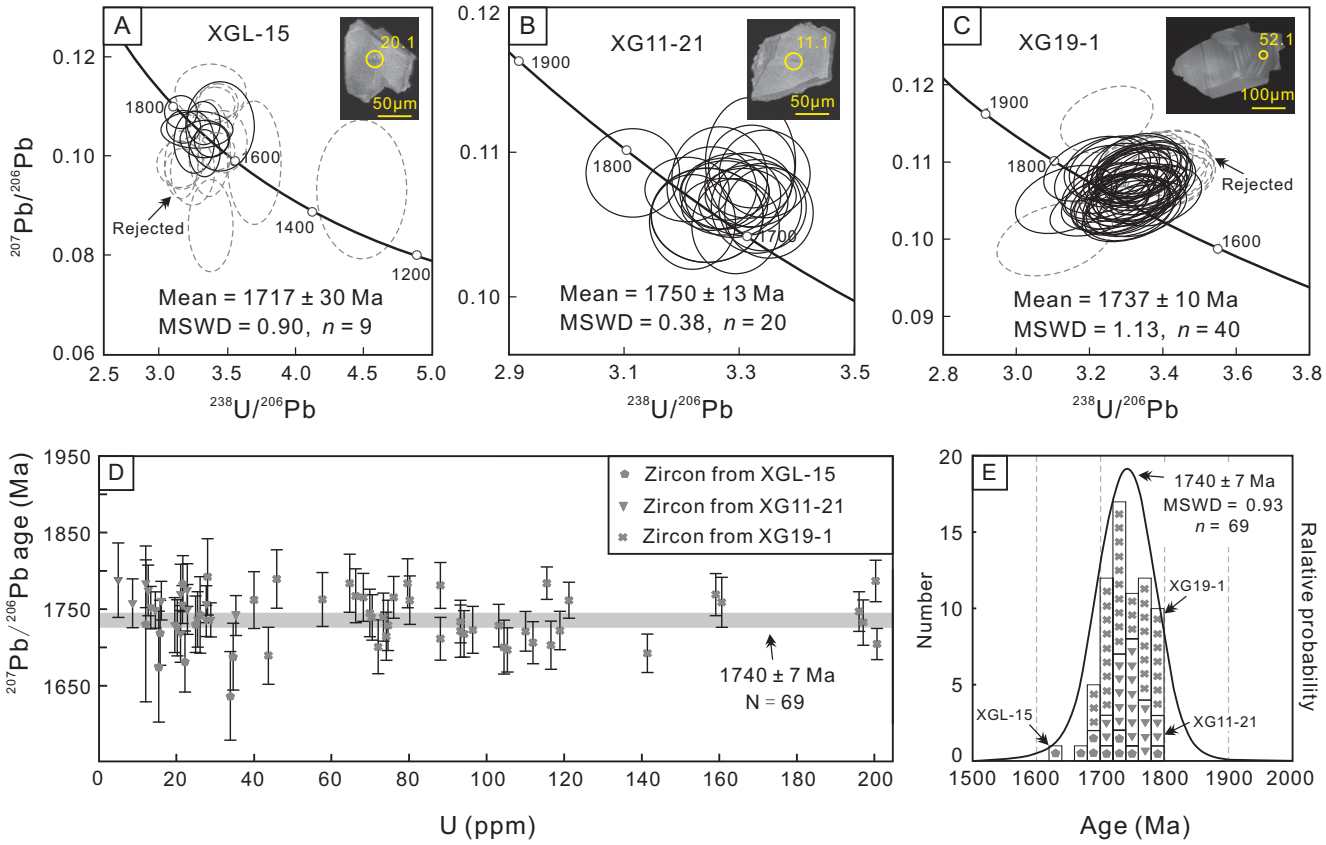

This is the peer-reviewed, final accepted version for American Mineralogist, published by the Mineralogical Society of America.
The published version is subject to change. Cite as Authors (Year) Title. American Mineralogist, in press.
DOI: https://doi.org/10.2138/am-2022-8501. http://www.minsocam.org/

Figure 6

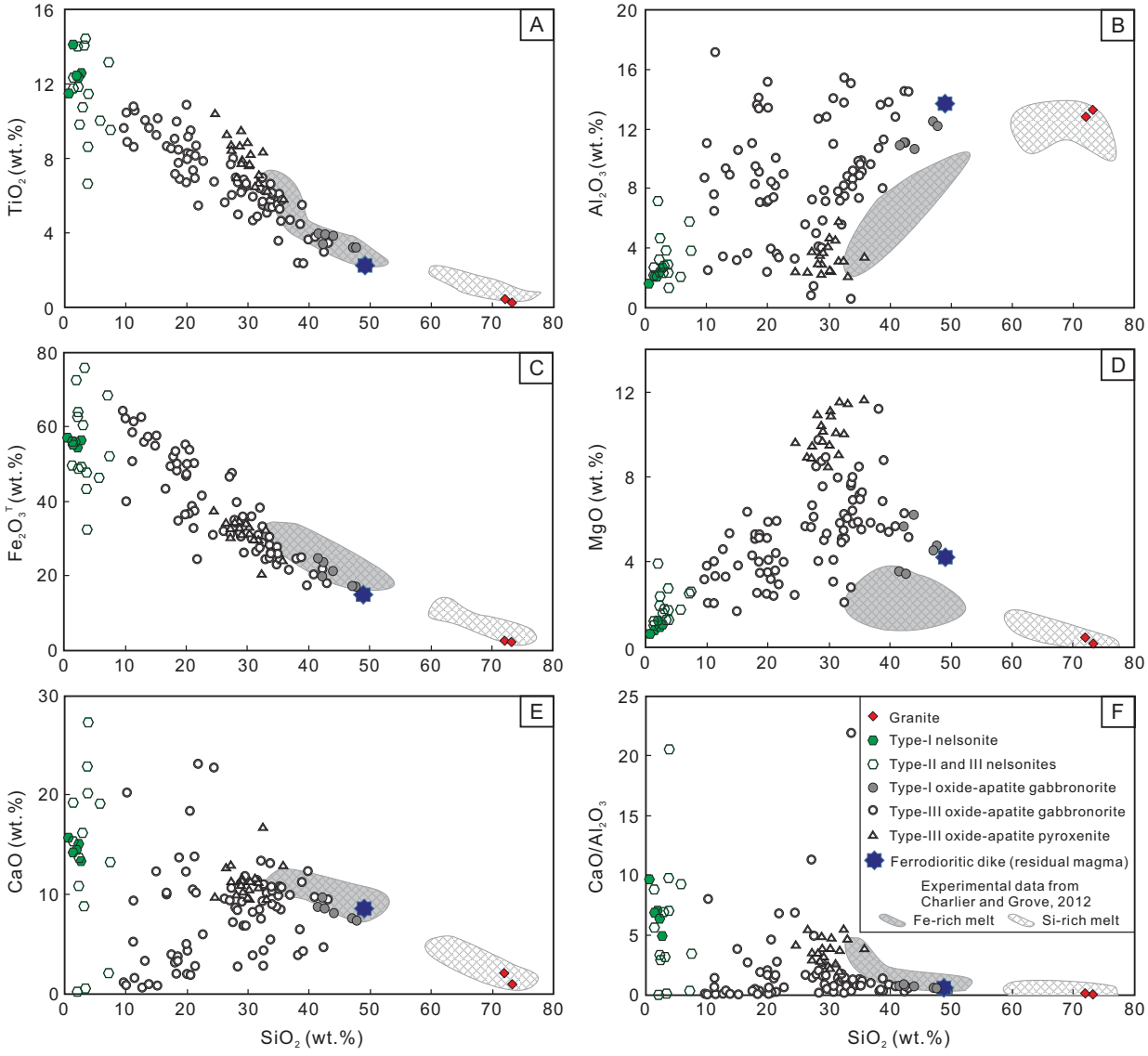

This is the peer-reviewed, final accepted version for American Mineralogist, published by the Mineralogical Society of America.
The published version is subject to change. Cite as Authors (Year) Title. American Mineralogist, in press.
DOI: https://doi.org/10.2138/am-2022-8501. http://www.minsocam.org/

Figure 7

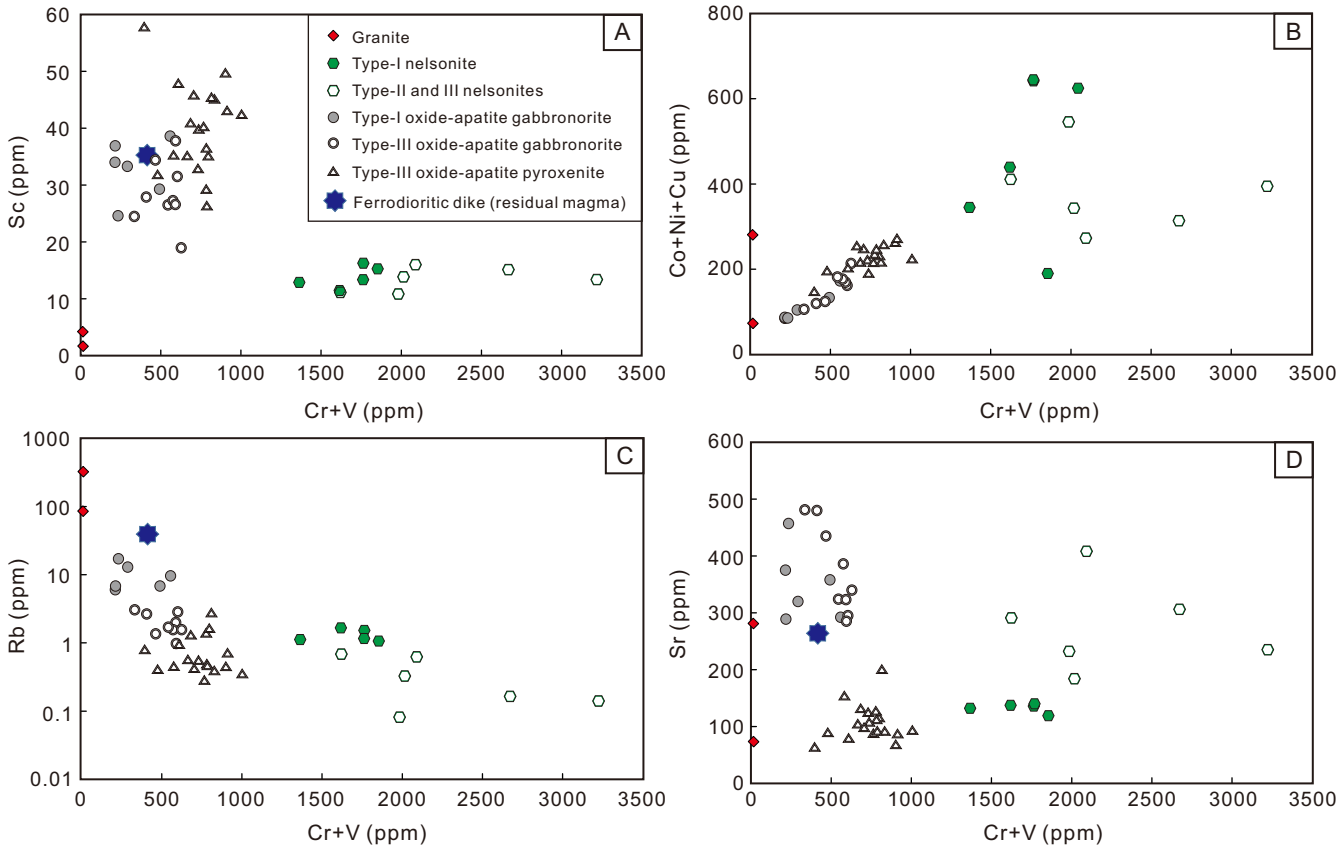

Figure 8

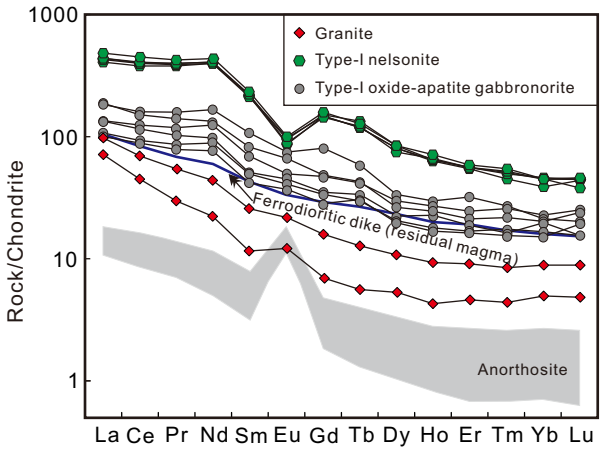

This is the peer-reviewed, final accepted version for American Mineralogist, published by the Mineralogical Society of America.
The published version is subject to change. Cite as Authors (Year) Title. American Mineralogist, in press.
DOI: https://doi.org/10.2138/am-2022-8501. http://www.minsocam.org/

Figure 9

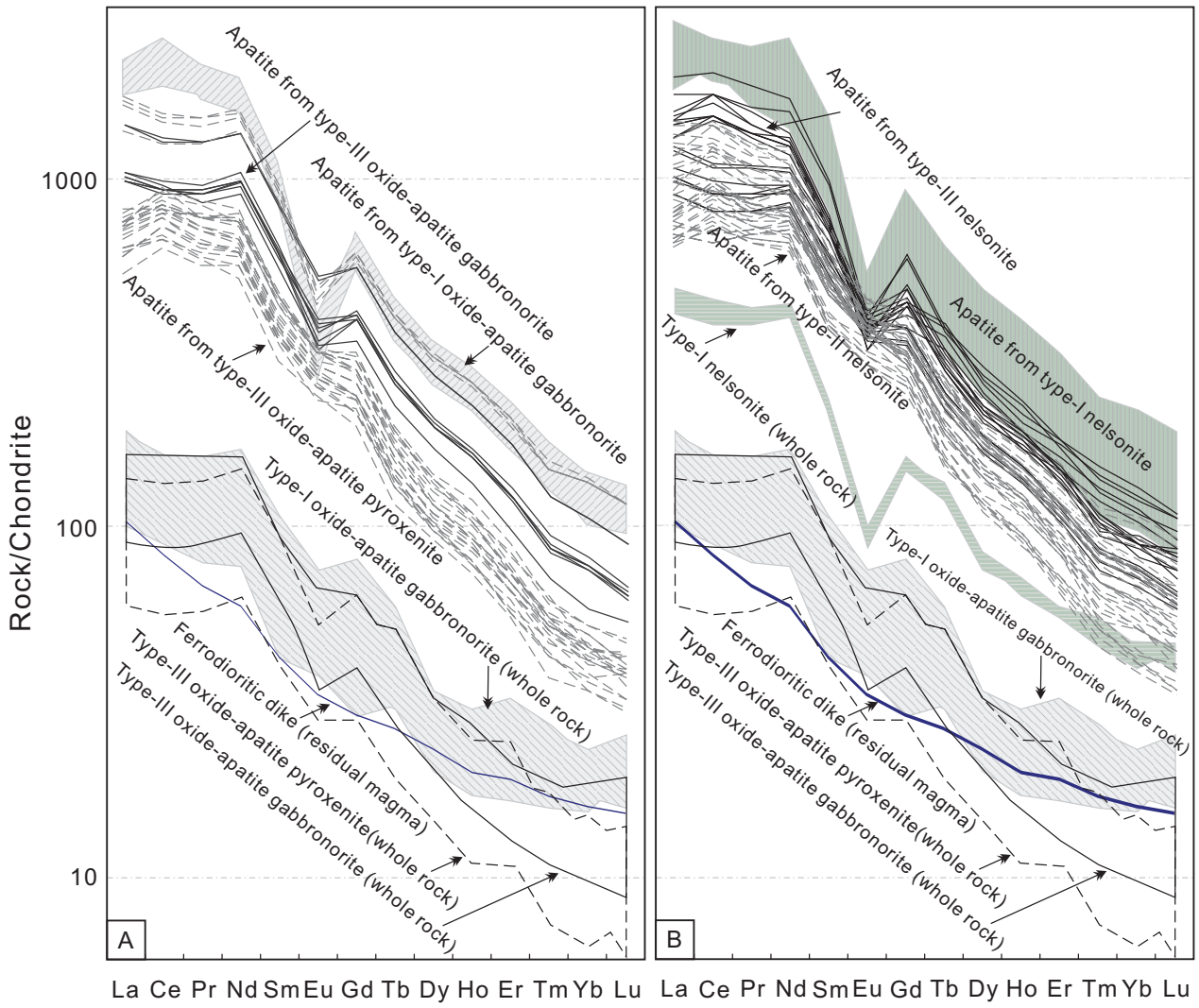

Figure 10